Journal of Naval Architecture and Marine Engineering
July, 2025
https://doi.org/10.3329/jname.v22i2.81890 http://www.banglajol.info

SLIP-DRIVEN MHD NANOFLUID FLOW OVER A CYLINDER: A COMPARATIVE STUDY OF STEADY AND UNSTEADY BOUNDARY LAYERS

Umme Hani[1], M. Ali[1], and Rehena Nasrin[2,*]
[1]Department of Mathematics, Chittagong University of Engineering and Technology, Chittagong, Bangladesh
[2]Department of Mathematics, Bangladesh University of Engineering and Technology, Dhaka, Bangladesh
*Correspondence: rehena@math.buet.ac.bd

Abstract:

This study aims to investigate the comparison of steady and unsteady MHD mixed convective nanofluid flow over a cylinder, taking into account various factors, including slip conditions, heat and mass transfer, heat generation, stretching ratio, thermal radiation, curvature, viscous dissipation, and chemical reactions. The analogous transformation technique is employed to transform nonlinear PDEs into a system of coupled ODEs, which are then solved using the Runge-Kutta fourth-order approach. The influences of numerous relevant parameters on the velocity, thermal, and concentration boundary layers (BLs) are illustrated graphically. Furthermore, the shear stress coefficient, Nusselt number, and Sherwood number are calculated for steady and unsteady flow conditions. The findings reveal that unsteady flow substantially influences the skin friction coefficient and the rate of mass transfer. Notably, the slip effect enhances these processes compared to steady flow; conversely, a contrary movement is observed in the heat transfer rate. It is observed that in unsteady flow conditions, the skin friction coefficient increases by 0.34%, and 0.04%, respectively due to the increase of power-law index and curvature; the Nusselt number decreases by approximately 0.2%, and 0.02% for increasing values of thermophoresis, and Brownian motion; as well as the Sherwood number decreases about 0.08%, and 0.05%, respectively for rising values of Schmidt number, and chemical reaction compared to steady flow. This research presents significant new insights into the thermal behavior of viscoelastic fluids, which have the potential to enhance heat transfer methodologies in industrial coating systems, chemical reactors, and polymer extrusion processes.

Keywords: Boundary layer, slip condition, MHD, Brownian motion, thermophoresis, chemical reaction, shear stress, unsteadiness

NOMENCLATURE:

	Dimensional		q_r	Radiative heat flux	$[Wm^{-2}]$
a	Stretching constant	-	q_w	Heat flux	$[Js^{-1}]$
b	Free stream rate constant	-	q_m	Mass flux	$[molm^{-3}]$
B_0	Transverse magnetic field strength	$[kgs^{-2}A^{-1}]$	T	Dimensional temperature	[K]
C	Dimensional concentration	$[kgm^{-3}]$	T_w	Wall temperature	[K]
C_p	Specific heat	$[Jkg^{-1}K^{-1}]$	T_∞	Free stream temperature	[K]
C_w	Wall concentration	$[kgm^{-3}]$	u	Velocity in the z-direction	$[ms^{-1}]$
C_∞	Free stream concentration	$[kgm^{-3}]$	U_w	Stretching velocity	$[ms^{-1}]$
D_B	Brownian diffusion coefficient	$[cm^2s^{-1}]$	U	Free stream velocity	$[ms^{-1}]$
D_T	Thermophoresis diffusion coefficient	$[m^2s^{-1}]$	v	Velocity in r-direction	$[ms^{-1}]$
g	Acceleration due to gravity	$[ms^{-2}]$		**Dimensionless**	
h_f	Convective heat transfer	$[Wm^{-2}K^{-1}]$	A	Stretching ratio parameter	-
K	Chemical reaction	$[molL^{-1}s^{-1}]$	A_1	Unsteadiness parameter	-
k	Thermal conductivity	$[Wm^{-1}K^{-1}]$	Bi	Biot number	-
m_1	Velocity slip	$[ms^{-1}]$	C_f	Skin friction coefficient	-
m_2	Thermal slip	[K]	Ec	Eckert number	-
m_3	Concentration slip	$[kgm^{-3}]$	$f(\eta)$	Dimensionless stream function	-

1813-8535 (Print), 2070-8998 (Online) © 2025 ANAME Publication. All rights reserved. Received on: April, 2025

Q_0	Heat source coefficient	[J]
$f''(\eta)$	Dimensionless velocity gradient	-
Gr	Thermal Grashof number	-
Gm	Mass Grashof number	-
K^*	Chemical reaction	-
M	Magnetic strength parameter	-
n	Power-law index	-
Nb	Brownian motion parameter	-
Nt	Thermophoresis parameter	-
Nu	Nusselt number	-
Q^*	Heat generation parameter	-
Rd	Radiation parameter	-
Re	Reynold’s number	-
Sc	Schmidt number	-
Sh	Sherwood number	-

Greek Symbols

α_f	Base fluid’s thermal diffusivity	[m^2s^{-1}]
β_T	Volumetric coefficient of thermal expansion	[K^{-1}]
$f'(\eta)$	Dimensionless velocity	$f'(\eta)$
β_c^*	Volumetric coefficient of concentration expansion	[$mol^{-1}L$]
μ_f	Dynamic viscosity	[$kgm^{-1}s^{-1}$]
ν	Base fluid’s kinematic viscosity	[kgm^{-3}]
ρ_f	Base fluid’s density	[kgm^{-3}]
σ	Electrical conductivity	[Sm^{-1}]
τ_w	Wall shear stress	[Nm^{-2}]
ψ	Stream function	[$m^{-2}s^{-1}$]
δ_2	Thermal slip parameter	-
δ_3	Concentration slip parameter	-
η	Similarity variable	-
$\theta(\eta)$	Dimensionless temperature	-
$\theta'(\eta)$	Rate of temperature change	-
κ	Curvature parameter	-
τ	Ratio of nanoparticle effective heat capacity and base fluid heat capacity	
$\phi(\eta)$	Dimensionless concentration	-
$\phi'(\eta)$	Rate of concentration	-

1. Introduction

In recent years, mixed convection flow, heat, and mass transference over cylindrical bodies has become an essential field with an extensive range of applications, such as heat exchangers, electronic cooling, chemical engineering, heat loss from piping, thermal energy storage devices, boilers, nuclear process systems, and more. Much theoretical and experimental research focuses on transportation processes' flow and heat transfer properties over cylindrical objects, widely using base fluids, such as oil, ethylene glycol, and water.

The study of nanofluids has garnered much attention lately since including nanoparticles would significantly improve the fluids' thermal conductivity during heat transfer. A nanofluid is a fluid with tiny volumetric amounts of nanoparticles (particles smaller than 100 nm). Nanofluids are innovative composites made of solid particles as small as nanometers mixed with traditional heat transfer fluids like motor oil, water, toluene, and ethylene glycol. The improvement of thermal conductivity by nanofluids has become more significant than the restricted heat transfer capabilities of the general fluids. While researching new coolants and cooling technologies, Choi (1995) was the first to introduce a novel fluid type known as nanofluid. A model for convective transfer in nanofluids was created by Buongiorno (2006), who concluded that there are seven potential mechanisms (particle accumulation, nanoparticle size, inertia, nanoparticle’s volume fraction, Magnus effect, Brownian motion, and thermophoresis) linking the convection of nanofluids to the current state of nanoparticles in the base fluid. Among those seven mechanisms, thermophoresis and Brownian motion are revealed to be crucial. Ali (2020) studied heat transfer analysis in nanofluids containing nanoparticles due to their high thermal conductivity and has demonstrated the properties of particles such as shape, size, temperature, etc.

The boundary layer (BL) is of great interest to researchers due to its importance in different fluid flow fields. Ludwig Prandtl first proposed the BL idea in (Tulapurkara, 2005). The BL theory shows that a stationary body's surface velocity is zero because of the no-slip requirement. Nevertheless, the BL is a thin layer containing the velocity that the non-viscous flow theory anticipated. Jarwal et al. (2023) categorized the impact of MHD mixed convection BL nanofluid (Ag/Cu with H_2O) flow through a permeable stretched cylinder in thermal radiation. Ahmed et al. (2014) determined how the impermeable stretching tube affects the flow in the BL and heat transmission properties because of the uncertainties in thermal conductivity and the dynamic viscosity of the nanofluid containing a heat source or sink. Jalili et al. (2023) examined the flow of BL nanofluid through the portable plate, considering the effects of internal heat generation, viscous dissipation, and radiation.

Assuming steady flow in BL flow and heat transmission studies is standard practice. However, unsteadiness became crucial in many engineering applications when the flow became time-dependent (Bachok et al. 2012). Mansur and Ishak (2016) investigated the unsteady nanofluid flow through a stretching/shrinking sheet. Tulu et al. (2024) looked at the influence of viscous dissipation on the MHD unsteady MWCNTs and Fe_3O_4 hybrid nanoparticles based on water flow through a rotating disk, considering the Cattaneo-Christov heat flux model. Investigation of the unsteady flow of nanofluid, made of silicon dioxide based on water, through a stretching cylinder, taking into account the effects of Joule heating and magnetic field, was carried out by Alia et al. (2024). Saranya et al. (2024) researched the dynamic behavior of unsteady flow of nanofluid (Fe_3O_4 with ester) over a contracting cylinder, considering the existence of heat generation, magnetic field, and homogeneous-heterogeneous reaction within a specific range of the unsteadiness parameter. The unsteady flow in the BL through a stretched/shrunk cylinder submerged in a nanofluid (Cu-water), considering suction impact, was examined by Dzulkifli et al. (2021). The main convective effects (permeability, uniform suction, and Joule heating) affecting heat transmission properties in Newtonian nanofluid (Al_2O_3 with water) MHD flow on a spinning disk were investigated by Bilal et al. (2024). Taking into account activation energy, which is observed in chemical processes, Choudhary et al. (2024) provided a numerical evaluation of unsteady flow, heat, and mass transport of conformist hybrid nanofluid (nanoparticles such as Cu and Al_2O_3 in the base fluid H_2O). Additionally, bioconvection flow with first-order slip and nonlinear radiation was considered.

The flow in the BL and heat transmission through a cylindrical stretched surface have been the focus of many researchers due to the many applications of cylindrical surfaces in engineering, contemporary technology, and industry. Reddy et al. (2018) investigated the impact of Prandtl number on the flow of fluid along a vertical cylinder that was uniformly heated using Bejan's heat function idea. The manner of a natural, unsteady convection BL nanofluid flow encircling a vertical cylinder was examined by Chamkha et al. (2013). The implicit finite-difference method was used to solve the equations regulating this flow. The incompressible viscous nanofluid passed into an upright circular cylinder was studied by Gholinia et al. (2018) while considering electric conductivity. This analysis has been deemed homogeneous and heterogeneous reactions, avoiding the effects of an inductive and electromagnetic field. A numerical comparison of unsteady nanofluid (TiO_2/H_2O) and hybrid nanofluid ($Ag+TiO_2/H_2O$) flows passing through a porous linear stretched cylinder in a porous medium with an oblique Lorentz force has been provided by Nandi and Barman (2024). Abbas et al. (2021) examined the flow at a hybrid nanofluid stagnation point over a rotating cylinder with a converging magnetic field. Umeshaiah et al. (2022) described the flow of a dusty nanofluid via a permeable stretched cylinder by considering the importance of the melting heat transfer event. They discovered that lowering the porosity parameter can lead to lower fluid- and dust-phase velocities.

Abbas et al. (2023) examined the impacts of thermal slip, thermal radiation, and viscous dissipation in the unsteady incompressible Sutterby fluid flow by comparing stretching cylinder and sheet with an induced magnetic field. To compare the steady and unsteady flow across a wedge surface, Reddy and Reddy (2020) conducted the impacts of multiple slip, chemical reaction, thermal radiation, thermophoresis, and Brownian motion in Buongiorno's Williamson nanofluid flow. Waqas et al. (2021) studied how heat radiation and viscosity dissipation affected the flow of a nanofluid over a permeable stretched cylinder, using engine oil as the base fluid and MoS_2 and Ag as nanoparticles. The consequences of heat generation and/or absorption on the movement of gyrotactic microorganisms carrying nanofluids along an inclined stretched cylinder that transfers mass and heat were investigated mathematically by Elbashbeshy et al. (2022). In the presence of three hybrid nanofluidic models (Xue, Yamada-Ota, and Tiwari Das), Shatnawi et al. (2022) analyzed the incompressible hybrid Casson nanofluid flow along an upright porous exponential stretched sheet, taking into account the effects of nonlinear radiation, heat production, and the induced magnetic field on slip effects. Under the influence of thermal radiation, Brownian motion, thermophoresis, and activation energy, Basit et al. (2024) assessed the heat and mass transfer rate of Maxwell nanofluid flow over a stretched medium.

Poornima et al. (2016) presented a mathematical model for an optically thick fluid that conducts a chemical reaction over an isothermal circular cylinder. In the existence of viscous dissipation, chemical reaction, and thermal radiation, Revathi and Poornima (2024) examined the Stefan blowing and convective boundary circumstances on the time-independent flow of an MHD nanofluid through a stretching sheet. Poornima et al. (2022) used the dimensionless master Prandtl equations to study the steady incompressible hybrid nanofluid (CuO and MgO) and an ordinary nanofluid stagnation-point flows along a stretched/shrunk cylinder. The investigation by Bhargavi et al. (2024) focused on three-dimensional, MHD carbon nanotubes floating in motor oil that create a nanofluid that flows through a stretched permeable surface with thermal slip.

Khan et al. (2025) presented a numerical study on a stretched sheet to explore the impacts of thermal radiation, Lorentz force, velocity, and thermal slips on Williamson nanofluid. They identified two distinct branches (dual solutions) due to the shrinking phenomenon and found that the upper branch was the most reliable following a stability analysis. Similarly, Zeeshan et al. (2025) analyzed the energy transition in thermal Casson hybrid nanofluid flow, considering the melting heat effect in a rocket engine nozzle. They detected a decline in the thermal field with increased thermal relaxation and melting factors.

From the above exploration, it should be noted that the comparison between steady and unsteady flow of boundary layer axisymmetric flow on a stretched cylinder under the combined impact of velocity slip, thermal slip, concentration slip, chemical reaction, viscous dissipation, mixed convection, magnetic field, and heat generation have not yet been endeavored to be examined. Thus, this investigation aims to observe how the shear stress coefficient, heat, and mass transfer rate vary for steady and unsteady flow, in addition to how heat production, velocity slip, thermal slip, concentration slip, and chemical reactions influence flow and heat transfer phenomena on cylindrical geometry with a magnetic field. The assumptions above are taken into consideration when assigning the convective conditions on boundaries. The governing flow equations are converted into a collection of non-dimensional forms using an appropriate similarity transform. A more suitable numerical technique was used in this analysis to get the results on the boundary value problem.

The novelty of this investigation is the comparison of steady and unsteady flow in the case of nanofluid flow along a cylinder using Buongiorno's model, which examines the consequences of thermal radiation, viscous dissipation, multiple slips, chemical reactions, and heat generation with a magnetic field on fluid flow, temperature and concentration phenomena within the BL region.

One of the many artificial methods created specially to control the boundary layer's nature is applying the MHD principle to the comparison of steady and unsteady flow. This technique transforms the boundary layer's structure and influences the flow field in the desired direction. Much attention has been focused on comparing steady and erratic flow in heat transfer over extending cylinders due to its industrial applications and substantial impact on numerous technological processes.

The current examination focuses on the subsequent research questions:

- ❖What parameters improve velocity, temperature, and concentration profiles within the boundary layer?
- ❖Is there a flow separation for the impacts of the relevant parameters?
- ❖What effects do the relevant parameters have on the shear stress coefficient, Nusselt number, and Sherwood number?
- ❖From the table of numerical values, which flow is suitable between steady and unsteady flow?

2. Mathematical Model

Considering a magnetic field, this study examines BL nanofluid flow on a cylindrical surface with the impacts of heat generation, viscous dissipation, and chemical reactions. The cylindrical coordinate system is assumed under the axisymmetric flow assumption for the mathematical representation. It is determined that the fluid velocities u and v are measured along the axial and radial directions of cylindrical coordinates, respectively.

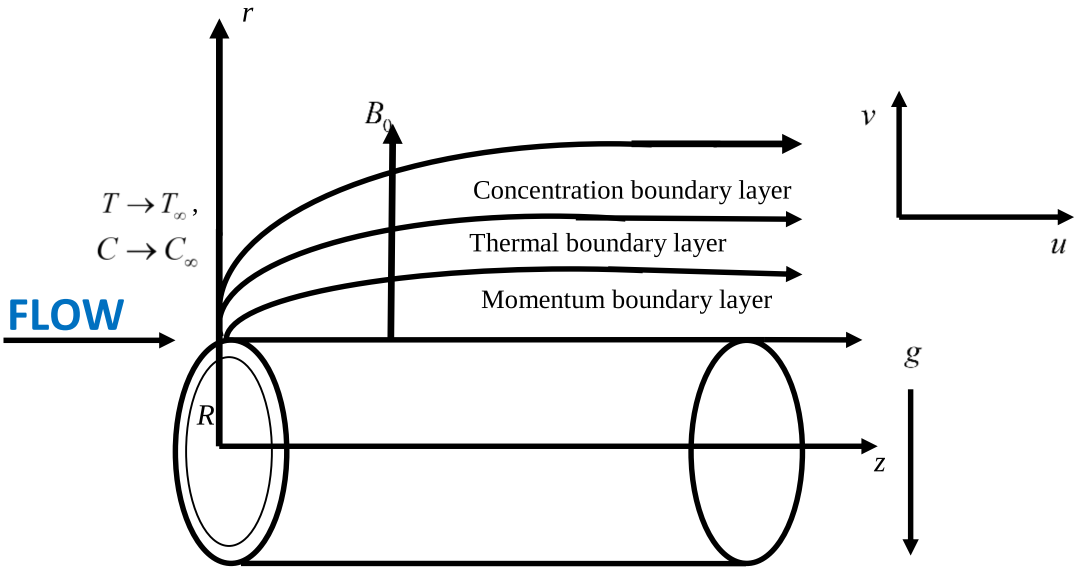

$$-k\frac{\partial T}{\partial r} = h_f(T_w - T) + m_2\frac{\partial T}{\partial r}, D_B\frac{\partial C}{\partial r} + \frac{D_T}{T_\infty}\frac{\partial T}{\partial r} = m_3\frac{\partial C}{\partial r}$$

Fig. 1: Fluid flow configuration

Fig. 1 illustrates how the strength of the magnetic field is applied along the radial direction of the cylinder while the nanofluid flow is considered along the z-axis. $U_w = \frac{az^n}{1-\omega t}$ is the stretching velocity of the cylinder, where $a > 0$ is the stretching constant and $U = \frac{bz^n}{1-\omega t}$ is the free stream velocity. Moreover, convective boundary conditions consider temperature, concentration, and velocity slip effects.

The study is predicated on the following assumptions:

- ❖Two-dimensional unsteady laminar mixed convective flow.
- ❖Fluid is incompressible, viscous, and electrically conducting.
- ❖Axisymmetric cylindrical coordinate system.

Given the presumptions above, the model's momentum, temperature, and concentration equations can be transcribed as Rajput et al. (2022):

$$\frac{\partial u}{\partial z} + \frac{v}{r} + \frac{\partial v}{\partial r} = 0, \tag{1}$$

$$\frac{\partial u}{\partial t} + u\frac{\partial u}{\partial z} + v\frac{\partial u}{\partial r} = U\frac{dU}{dz} + \nu\left(\frac{\partial^2 u}{\partial r^2} + \frac{1}{r}\frac{\partial u}{\partial r}\right) - \frac{\sigma B_0^2}{\rho_f}\left(u - U\right) + \beta_T g\left(T - T_\infty\right) + \beta_c^* g\left(C - C_\infty\right), \tag{2}$$

$$\begin{aligned}\frac{\partial T}{\partial t} + u\frac{\partial T}{\partial z} + v\frac{\partial T}{\partial r} = \alpha_f\left(\frac{\partial^2 T}{\partial r^2} + \frac{1}{r}\frac{\partial T}{\partial r}\right) + \tau\left[D_B\frac{\partial C}{\partial r}\frac{\partial T}{\partial r} + \frac{D_T}{T_\infty}\left(\frac{\partial T}{\partial r}\right)^2\right] - \frac{1}{\rho C_p r}\frac{\partial\left(rq_r\right)}{\partial r} + \frac{Q_0}{\rho C_p}\left(T - T_\infty\right) \\ + \frac{\nu}{C_p}\left(\frac{\partial u}{\partial r}\right)^2\end{aligned}, \tag{3}$$

$$\frac{\partial C}{\partial t} + u\frac{\partial C}{\partial z} + v\frac{\partial C}{\partial r} = D_B\left[\frac{\partial^2 C}{\partial r^2} + \frac{1}{r}\frac{\partial C}{\partial r}\right] + \frac{D_T}{T_\infty}\left[\frac{\partial^2 T}{\partial r^2} + \frac{1}{r}\frac{\partial T}{\partial r}\right] - K\left(C - C_\infty\right), \tag{4}$$

Where and v are the velocity ingredients along z and r directions, t denotes the time, U is the free stream velocity, T and T_∞ are the dimensional and the free stream temperature, C and C_∞ and the dimensional and the free stream concentration, g is the acceleration due to gravity, ν is the base fluid's kinematic viscosity, σ is the electrical conductivity, ρ_f is the base fluid's density, B_0 denotes the transverse magnetic field strength, β_T and β_c^* are the volumetric coefficient of thermal expansion and concentration expansion, α_f is the base fluid's thermal diffusivity, τ is the ratio of nanoparticle effective heat capacity and base fluid heat capacity, D_B and D_T are the Brownian and the thermophoresis diffusion coefficient, q_r is the radiative heat flux, C_p is the specific heat, ρC_p is the nanofluid heat capacity, Q_0 is the heat source coefficient, and K is the chemical reaction.

The thermal radiative heat flux (Rosseland, 1931) is given by

$$q_r = -\frac{4\sigma^*}{3k^*}\frac{\partial\left(T^4\right)}{\partial r}, \tag{5}$$

Where σ^* is the Stefan-Boltzmann constant and k^* is the mean absorption coefficient. Assume the fluid's temperature is proportional to the absolute temperature raised to the fourth power.

The following T^4 can be expanded approximately while ignoring higher-order terms using the Taylor series expansion:

$$T^4 = 4T_\infty^3 T - 3T_\infty^4, \tag{6}$$

Inserting Eq. (6) into Eq. (5), then q_r becomes

$$q_r = -\frac{4\sigma^*}{3k^*}\frac{\partial}{\partial r}\left(4T_\infty^3 T\right), \tag{7}$$

As a result, Eq. (3) can be expressed as

$$\frac{\partial T}{\partial t}+u\frac{\partial T}{\partial z}+v\frac{\partial T}{\partial r}=\alpha_f\left(\frac{\partial^2 T}{\partial r^2}+\frac{1}{r}\frac{\partial T}{\partial r}\right)+\tau\left[D_B\frac{\partial C}{\partial r}\frac{\partial T}{\partial r}+\frac{D_T}{T_\infty}\left(\frac{\partial T}{\partial r}\right)^2\right]+\frac{16\sigma^* T_\infty^3}{3\rho C_p k^*}\left[\frac{\partial^2 T}{\partial r^2}+\frac{1}{r}\frac{\partial T}{\partial r}\right], \qquad (8)$$

$$+\frac{Q_0}{\rho C_p}\left(T-T_\infty\right)+\frac{\nu}{C_p}\left(\frac{\partial u}{\partial r}\right)^2$$

For the governing equations (2), (4), and (8), the following boundary conditions are given according to Narender et al. (2021):

$$u=U_w+m_1\frac{\partial u}{\partial r},\ v=0,\ -k\frac{\partial T}{\partial r}=h_f(T_w-T)+m_2\frac{\partial T}{\partial r},\ D_B\frac{\partial C}{\partial r}+\frac{D_T}{T_\infty}\frac{\partial T}{\partial r}=m_3\frac{\partial C}{\partial r}\ \text{ at } r=R$$

$$u\to U,\ T\to T_\infty,\ C\to C_\infty \quad \text{at } r\to\infty. \qquad (9)$$

Where m_1, m_2, and m_3 are the velocity slip parameter, thermal slip parameter, and concentration slip parameter, respectively. k is the thermal conductivity, h_f is the convective heat transfer. In the absence of slip flow, m_1, m_2, and m_3 become zero.

Transforming the collection of dimensional PDEs into dimensionless ODEs requires applying similarity transformations in Eqs. (2), (4), (8), and the boundary conditions shown in Eq. (9):

$$u=\frac{1}{r}\frac{\partial\psi}{\partial r},\quad v=-\frac{1}{r}\frac{\partial\psi}{\partial z},\quad \psi=\left(\frac{\nu b}{1-\omega t}\right)^{1/2} z^{n+1/2}Rf(\eta),\quad \eta=\frac{r^2-R^2}{2R}\left(\frac{b}{\nu(1-\omega t)}\right)^{1/2} z^{n-1/2},$$

$$T=T_\infty+T_w\left(\frac{bz^n}{2\nu(1-\omega t)^2}\right)\theta(\eta),\ \text{ and }\ C=C_\infty+C_w\left(\frac{bz^n}{2\nu(1-\omega t)^2}\right)\phi(\eta). \qquad (10)$$

Here, T_w, and C_w represent the cylinder wall temperature and concentration, respectively.

Using Eq. (10) in Eqs. (2), (4), (8), and (9), one can calculate the following ODEs:

$$\left(1+2\kappa\eta\right)f'''+2\kappa f''-nf'^2+\frac{n+1}{2}ff''-\left(A_1+M\right)f'+M-\frac{A_1}{2}\eta f''+Gr\theta+Gm\phi+n=0, \qquad (11)$$

$$\left(1+\frac{4}{3}Rd\right)\left[\left(1+2\kappa\eta\right)\theta''+2\kappa\theta'\right]-Pr$$

$$\left[\frac{A_1}{2}\eta\theta'+2A_1\theta+nf'\theta-\frac{n+1}{2}f\theta'-\left(1+2\kappa\eta\right)\left(Nb\theta'\phi'+Nt\theta'^2\right)-Q^*\theta-Ec\left(1+2\kappa\eta\right)f''^2\right]=0, \qquad (12)$$

$$\left(1+2\kappa\eta\right)\phi''+2\kappa\phi'+\frac{Nt}{Nb}\left[\left(1+2\kappa\eta\right)\theta''+2\kappa\theta'\right]+Sc\left(\frac{n+1}{2}f\phi'-nf'\phi--2A_1\phi-\frac{A_1}{2}\eta\phi'-K^*\phi\right)=0, \qquad (13)$$

With boundary conditions:

$$f'=A+\delta_1 f'',\ \left(1+\delta_2\right)\theta'=-Bi\left(1-\theta\right),\ Nb\left(1-\delta_3\right)\phi'+Nt\theta'=0\ \text{ at } \eta=0$$

$$f'\to 1,\ \theta\to 0,\ \phi\to 0 \quad \text{at } \eta\to\infty. \qquad (14)$$

Where $\kappa=\left(\frac{\nu}{UR^2}\right)^{1/2}$ is the curvature parameter, $A_1=\frac{\omega}{U(1-\omega t)}$ is the unsteadiness parameter, $M=\frac{\sigma B_0^2}{\rho_f U}$ is the magnetic strength parameter, $Gr=\frac{\beta_T g\,(T_w-T_\infty)}{U^2}$ is the thermal Grashof number, $Gm=\frac{\beta_C^* g(C_w-C_\infty)}{U^2}$ is the mass Grashof number, $Pr=\frac{\nu}{\alpha_f}$ is the Prandtl number, $Rd=\frac{4\sigma^* T_\infty^3\alpha_f}{k^* k_f}$ is the radiation parameter, $Nb=\frac{\tau U D_B C_w}{2\nu^2(1-\omega t)}$ is the Brownian motion, $Nt=\frac{\tau U D_T T_w}{2\nu^2 T_\infty(1-\omega t)}$ is the thermophoresis, $Ec=\frac{2U\nu}{C_p T_w}$ is the Eckert number, $Q^*=\frac{Q_0}{\rho_f C_p U}$ is the heat generation parameter, $Sc=\frac{\nu}{D_B}$ is the Schmidt number, $K^*=\frac{K}{U}$ is the chemical reaction parameter, $A=\frac{a}{b}$ is the Stretching ratio parameter, $\delta_1=\frac{m_1}{R\kappa}$ is the velocity slip parameter, $Bi=\frac{\kappa R h_f}{k}$ is the Biot number, $\delta_2=\frac{m_2}{k}$ is the thermal slip parameter, and $\delta_3=\frac{m_3}{D_B}$ is the concentration slip parameter, n is the power-law index.

The physical quantities, particularly the skin friction coefficient (C_f), Nusselt number (*Nu*), Sherwood number (Sh), are stated as follows for engineering purposes by Mabood and Shateyi (2019):

$$C_f=\frac{\tau_w}{\rho_f U_W^2},\quad Nu=\frac{z\,q_w}{k(T_w-T_\infty)},\ \text{and}\ \ Sh=\frac{z\,q_m}{D_B(C_w-C_\infty)} \qquad (15)$$

Here, τ_w, q_w, and q_m represent the wall shear stress, heat flux, and mass flux, respectively. According to (Ali et al. 2021, Ali et al. 2023, Hossain et al. 2025) , three quantities are defined as follows:

$$\tau_w = -\mu_f \left(\frac{\partial u}{\partial r}\right)_{r=R}, q_w = -k\left(\frac{\partial T}{\partial r}\right)_{r=R} - \frac{4\sigma^*}{3k^*}\left(\frac{\partial T^4}{\partial r}\right)_{r=R}, \text{ and } q_m = -D_B\left(\frac{\partial C}{\partial r}\right)_{r=R} \tag{16}$$

Here μ_f is the base fluid's dynamic viscosity.

Substituting Eqs. (10) and (16) into Eq. (15) to obtain the non-dimensional form of skin friction coefficient, Nusselt number, and Sherwood number:

$$\sqrt{Re}C_f = -f''(0), \frac{Nu}{\sqrt{Re}} = -\left(1+Rd\right)\theta'(0), \text{ and } \frac{Sh}{\sqrt{Re}} = -\phi'(0), \tag{17}$$

where, $Re = \dfrac{U_w a^3 z}{\nu b^3}$ is the Reynolds number.

3. Solution Procedure

Equations (11) through (13) present reduced ODEs, whereas Equation (14) presents boundary conditions. The Runge-Kutta fourth-order approach is used in MATLAB software code to solve these ODEs numerically. This method, particularly the fourth-order variant, is known for its superior accuracy in solving ODEs compared to other numerical methods. Its versatility allows it to handle both first-order and higher-order equations effectively. Additionally, it exhibits stability properties that keep numerical solutions bounded and prevent significant divergence, ensuring reliable results across various integration steps. These are the first-order ODEs that were obtained with the presumptive set of new variables:

$$(y_1, y_2, y_3, y_4, y_5, y_6, y_7)^T = (f, f', f'', \theta, \theta', \phi, \phi'), \tag{18}$$

$$y_3' = -\frac{1}{(1+2\kappa\eta)}[2\kappa y_3 - ny_2{}^2 + \frac{n+1}{2}y_1 y_3 - \left(A_1 + M\right)y_2 + M - \frac{A_1}{2}\eta y_3 + Gry_4 + Gmy_6 + \mathrm{n}], \tag{19}$$

$$\begin{gathered} y_5' = \frac{Pr}{(1+2\kappa\eta)}\left(1+\frac{4}{3}Rd\right)^{-1}[\frac{A_1}{2}\eta y_5 + 2A_1 y_4 - \frac{n+1}{2}y_1 y_5 + ny_2 y_4 - (1+2\kappa\eta) \\ (\mathrm{Nby_5 y_7} + \mathrm{Nty_5^2}) - Q^* y_4 - \mathrm{Ec}(1+2\kappa\eta)\,\mathrm{y_3^2}] - \frac{1}{(1+2\kappa\eta)}2\kappa y_5 \end{gathered}, \tag{20}$$

$$\begin{gathered} y_7' = -\frac{1}{(1+2\kappa\eta)}[2\kappa\,\mathrm{y}_7 + Sc\left(\frac{n+1}{2}y_1 y_7 - ny_2 y_6 - -2A_1 y_6 - \frac{A_1}{2}\eta y_7 - K^* y_6\right) \\ + \frac{Pr * Nt}{Nb}\left(1+\frac{4}{3}Rd\right)^{-1}\{(\frac{A_1}{2}\eta y_5 + 2A_1 y_4 - \frac{n+1}{2}y_1 y_5 + ny_2 y_4 - Q^* y_4) \\ -(1+2\kappa\eta)\{(Nby_5 y_7 + Nty_5{}^2) - Ec(1+2\kappa\eta)y_3^2\}\}] \end{gathered}, \tag{21}$$

With boundary conditions

$$y_1 = 0, y_2 = A + \delta_1 y_3, y_4 = 0, \left(1+\delta_2\right)y_5 = -Bi(1-y_4), \; Nb\left(1-\delta_3\right)y_7 + Nty_5 = 0 \text{ at } \eta = 0$$

$$y_2 \to 1, \; y_4 \to 0, \; y_6 \to 0 \quad \text{at } \eta \to \infty.$$

4. Results and Discussion

The effect of developing physical parameters on numerically determined momentum, thermal, and concentration profiles is examined in this section. It investigates how various embedding variables, including magnetic strength $M\left(0.0 \le M \le 9.0\right)$ slip factors ($0.0 \le \delta_1 \le 0.3$, $1.0 \le \delta_2 \le 7.0$, $0.0 \le \delta_2 \le 0.6$), Eckert number Ec $\left(0.0 \le Ec \le 1.5\right)$, curvature κ $\left(0.0 \le \kappa \le 0.6\right)$, thermal Grashof number Gr $\left(0.3 \le Gr \le 3.3\right)$, mass Grashof number $Gm\left(0.3 \le Gm \le 9.3\right)$, Prandtl number Pr $\left(0.15 \le Pr \le 0.45\right)$, heat generation Q^* $\left(0.0 \le Q^* \le 0.9\right)$, Brownian motion $Nb\left(0.1 \le Nb \le 0.4\right)$, thermophoresis $Nt\left(0.0 \le Nt \le 0.9\right)$, Schmidt number Sc$\left(1.0 \le Sc \le 4.0\right)$, chemical reaction $K^*\left(1.0 \le K^* \le 7.0\right)$, radiation $Rd\left(0.8 \le Rd \le 2.6\right)$, stretching ratio A $\left(0.0 \le A \le 1.0\right)$, Power-law index n$\left(1.0 \le n \le 4.0\right)$, Biot number Bi $\left(0.1 \le Bi \le 0.4\right)$, and unsteadiness $A_1(0.0 \le A_1 \le 0.6)$ affect dimensionless velocity, temperature, and concentration distributions. The selection of ranges for physical parameters relies on physical relevance, existing literature, mathematical stability, and sensitivity analysis. These ranges aim to reflect real-world systems while avoiding singularities, enabling meaningful comparisons between steady and unsteady regimes and different transport mechanisms. The study analyses how these factors affect the system's flow, thermal, and mass behaviour. It also examines how these values affect the shear stress coefficient, heat transfer, and mass transfer rate. The information is presented in graphs and tables, which provide the results in a visual representation for simpler comprehension and interpretation.

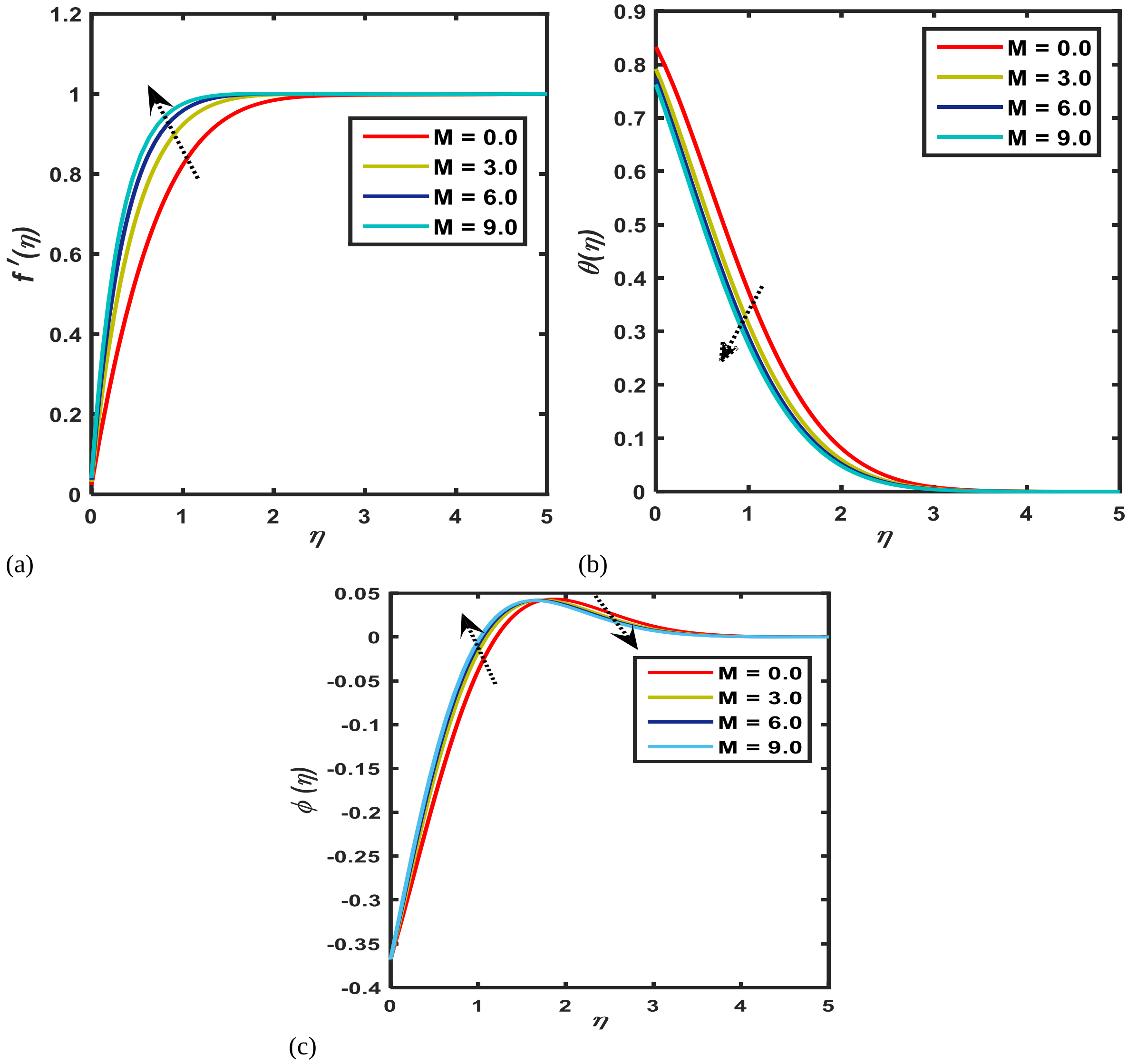

(a) (b)

(c)

Fig. 2: (a) f', (b) θ, and (c) ϕ profiles for the impact of magnetic strength with $n = 1.0$, $Gr = 0.3$, $Gm = 0.3$, $\kappa = 0.1$, $Ec = 0.01$, $Rd = 0.01$, $Pr = 1.0$, $Nt = 0.2$, $Q^* = 1.0$, $Sc = 1.0$, $K^* = 1.0$, $Nb = 0.2$, $A = 0.01$, $\delta_1 = 0.01$, $\delta_2 = 0.01$, $\delta_3 = 0.01$, $A_1 = 0.01$.

4.1 Influence of magnetic strength (M)

The impact of magnetic strength on the f', θ, and ϕ profiles in the BL are portrayed in Fig. 2. It is seen from Figs. 2(a) and 2(b) that the momentum BL thickness decelerates while the thermal BL thickness accelerates with a development in the values of M. On the other hand, the concentration BL thickness enhances near the cylindrical surface. It decreases far from the surface within the BL depicted in Fig. 2(c). With increasing levels of M, a weak

Lorentz force is produced when the free stream velocity exceeds the stretching velocity. According to the research, a weak Lorentz force is produced as the free stream velocity dominates the BL as the magnetic parameter rises. As a result, the fluid's velocity increases, and the fluid particles' resistance falls, which lowers the temperature profile. Also, the concentration profile grows considerably close to the cylinder surface as the magnetic strength increases.

4.2 Influence of curvature (κ)

The impact of the curvature parameter on the velocity, temperature, and concentration profiles in the BL is depicted in Fig. 3. In Figs. 3(a), 3(b), and 3(c), it is observed that momentum, thermal, and concentration BL thickness diminish with values of the curvature parameter. From a physical viewpoint of the curvature parameter, it has been noted that the fluid velocity has an instigating nature for high κ values. The converse association between a fluid's curvature and speed means that the fluid's velocity decreases when the curvature parameter increases. The momentum, thermal, and concentration BL thicknesses all decrease close to the cylindrical surface as a result, which is significant.

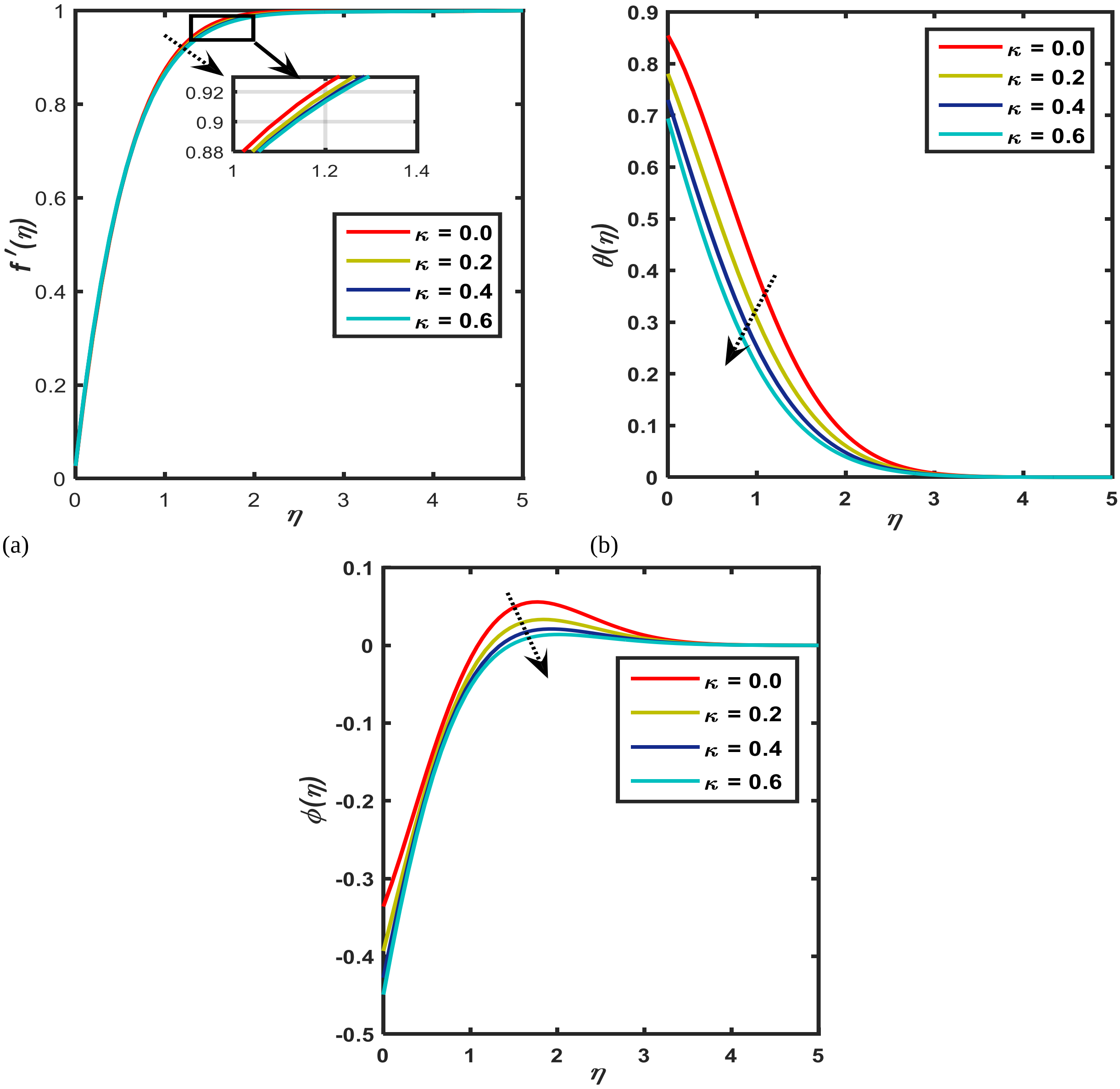

(a) (b)

(c)

Fig. 3: (a) f', (b) θ, and (c) ϕ profiles for impact of curvature with $M = 1.0$, $Gr = 0.3$, $Gm = 0.3$, $\kappa = 0.1$, $Ec = 0.01$, $Rd = 0.01$, $Pr = 1.0$, $Nt = 0.2$, $Q^* = 1.0$, $Sc = 1.0$, $K^* = 1.0$, $Nb = 0.2$, $A = 0.01$, $n = 1.0$, $\delta_1 = 0.01$, $\delta_2 = 0.01$, $\delta_3 = 0.01$, $A_1 = 0.01$.

4.3 Influence of Brownian motion (*Nb*)

Fig. 4 describes the consequences of the Brownian motion parameter on the concentration profile. It shows that the concentration profile and BL thickness increase near the cylindrical surface and decline far away from the surface. The random movement of adjourned nanoparticles in a base fluid is called Brownian motion, and it is mainly driven by the base fluid's rapidly moving molecules. Brownian motion is correlated with nanoparticle size and frequently manifests as aggregates. Consequently, the thickness of concentration BL increases near the cylindrical surface for increasing values of the Brownian motion parameter. As *Nb* increases, the concentration difference at the free stream decreases more rapidly, and the concentration boundary layer at the boundary drops with Nb. This is because *Nb* increases the Brownian motion coefficient and strengthens the Brownian motion of the nanoparticles.

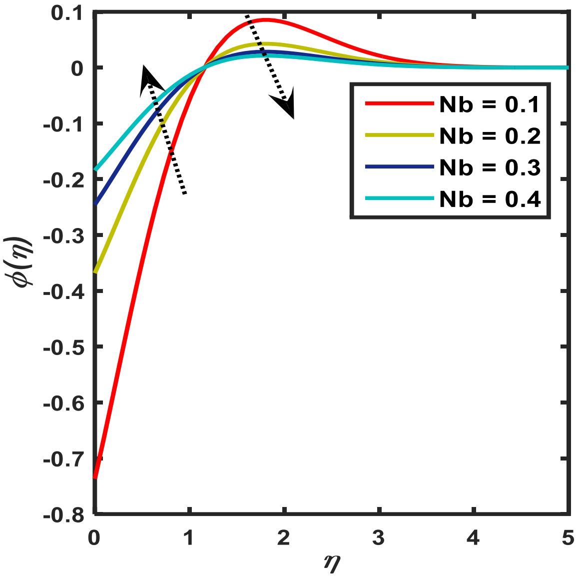

Fig. 4: ϕ profile for impact of Brownian motion with $M = 1.0$, $n = 1.0$, $Gr = 0.3$, $Gm = 0.3$, $\kappa = 0.1$, $Ec = 0.01$, $Rd = 0.01$, $Pr = 1.0$, $Nt = 0.2$, $Q^* = 1.0$, $Sc = 1.0$, $K^* = 1.0$, $A = 0.01$, $\delta_1 = 0.01$, $\delta_2 = 0.01$, $\delta_3 = 0.01$, $A_1 = 0.01$.

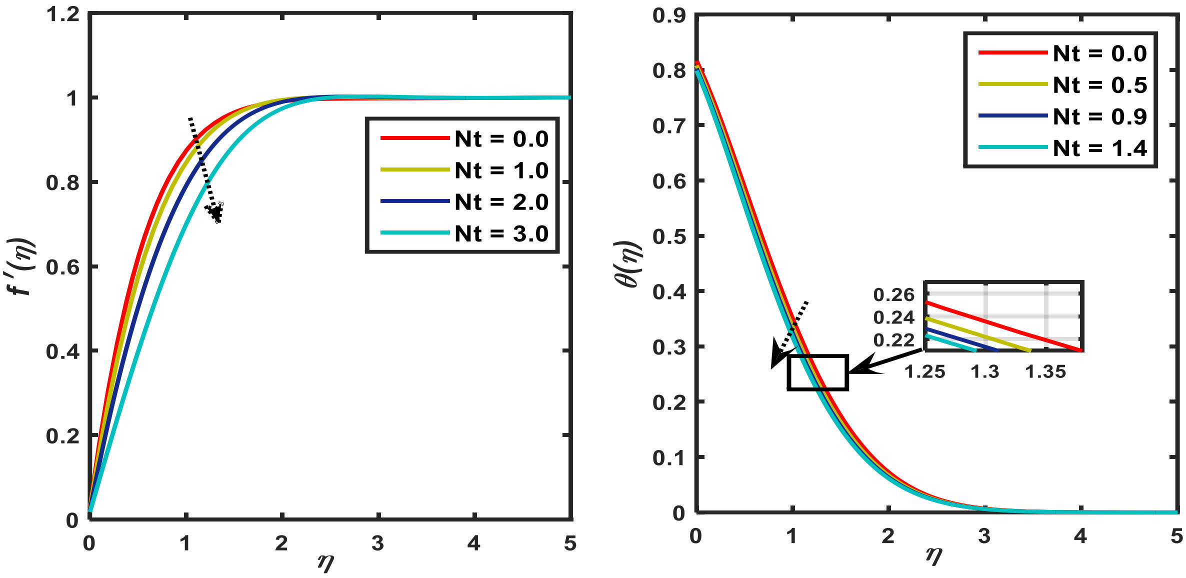

(a)

(b)

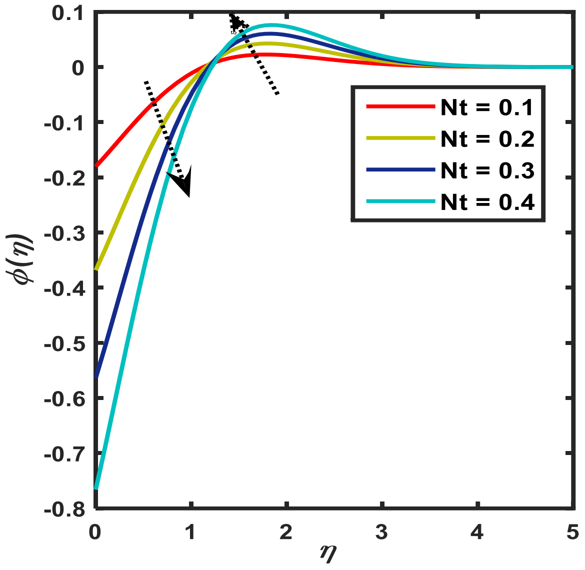

(c)

Fig. 5: (a) f', (b) θ, and (c) ϕ profiles for impact of thermophoresis with $M = 1.0$, $n = 1.0$, $Gr = 0.3$, $Gm = 0.3$, $\kappa = 0.1$, $Ec = 0.01$, $Rd = 0.01$, $Pr = 1.0$, $Q^{*} = 1.0$, $Sc = 1.0$, $K^{*} = 1.0$, $Nb = 0.2$, $A = 0.01$, $\delta_1 = 0.01$, $\delta_2 = 0.01$, $\delta_3 = 0.01$, $A_1 = 0.01$.

4.4 Influence of thermophoresis (*Nt*)

The consequences of thermophoresis on the velocity, temperature, and concentration profile are depicted in Fig. 5. Figs. 5(a) and 5(b) show that velocity and temperature profiles decrease in the BL region for higher values of the thermophoresis. However, in Fig. 5(c), the concentration profile (concentration BL thickness) declines near the cylindrical surface and surges far from the surface. The mechanics behind this phenomenon is that the temperature differential creates a thermophoretic force close to the stretching surface. When the temperature gradient is less, this force results in a very slow flow. As *Nt* increases, this force—which aids in transferring heat from the heated wall to the bulk fluid becomes stronger, thickening the concentration boundary layers far from the surface. The fluid is brought closer to the stretched sheet and is less heated. Consequently, as the values of thermophoresis increase, the BL thickness of θ and ϕ drops near the surface.

4.5 Influence of heat generation (Q*)

Fig. 6 exemplifies the impacts of the heat generation parameter on temperature and concentration profiles. In Fig. 6(a), θ and thermal BL thickness are improved for higher values of the heat generation parameter. However, the concentration profile and BL thickness diminish near the cylindrical surface and increase with distance from the surface, as illustrated in Fig. 6(b). Heat is produced when the heat generation parameter is positive; when it is not, heat is absorbed. A heat absorption coefficient physically lowers the fluid's temperature. This is significant because energy from other sources is converted to thermal energy when heat is created in a fluid. The temperature and the thermal BL thickness may increase due to heat generation. When there is a magnetic parameter present, because of the resistive force, a specific quantity of heat energy is simultaneously stored in the thermal and concentration boundary layers far away from the surface, together with the heat-generating parameter. The internal heat generation significantly affects the concentration profile due to the interplay between thermal and solutal transport mechanisms in nanofluid flow over a cylinder by raising local temperatures, strengthening thermophoretic and Brownian diffusion, leading to wider and possibly flattened concentration boundary layers, and producing marked differences in behavior between steady and unsteady flow regimes.

4.6 Influence of chemical reaction (*K**)

The effects of chemical reaction on the concentration profile are portrayed in Fig. 7. It shows that the concentration profile and the concentration BL thickness rise near the cylindrical surface and drop in distance from the surface. According to the physics of chemical reactions, the temperature on the surface decreases for larger values of chemical reaction parameters because there is less diffusivity in the flow field. However, more interaction in species concentration is implied by lower diffusivity. Chemical reactions are essential in manufacturing, medicine, and other fields. Note that K essentially represents the isothermal rate of a chemical reaction. The reaction rate can be accelerated by increasing R to promote molecular mass transfer.

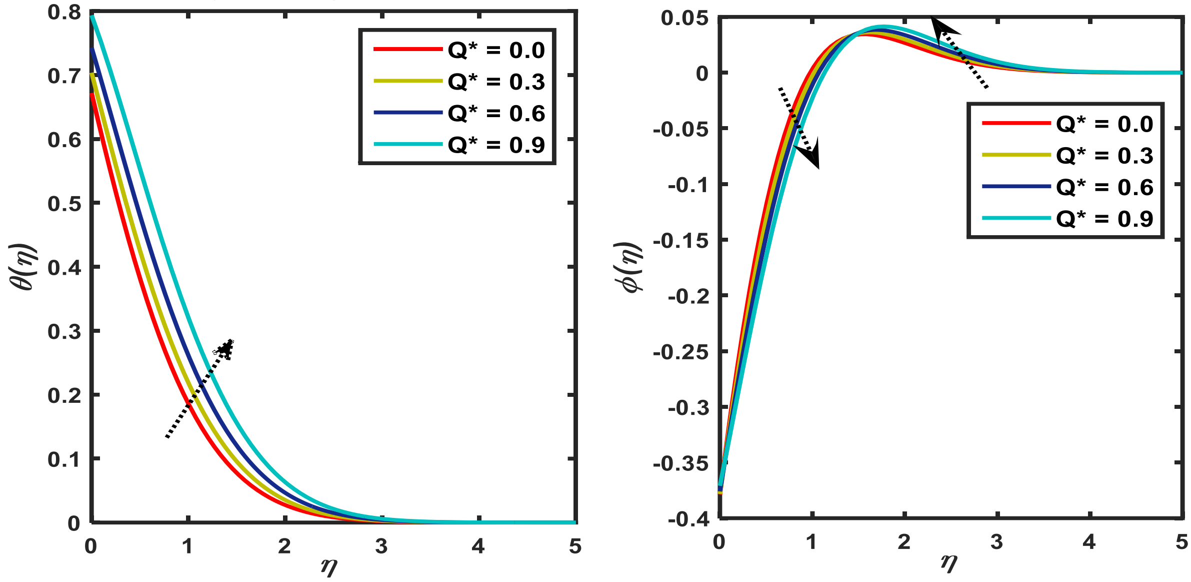

(a) (b)

Fig. 6: (a) θ, and (b) ϕ profiles for impact of heat generation with $M = 1.0$, $n = 1.0$, $Gr = 0.3$, $Gm = 0.3$, $\kappa = 0.1$, $Ec = 0.01$, $Rd = 0.01$, $Pr = 1.0$, $Nt = 0.2$, $Sc = 1.0$, $K^* = 1.0$, $Nb = 0.2$, $A = 0.01$, $\delta_1 = 0.01$, $\delta_2 = 0.01$, $\delta_3 = 0.01$, $A_1 = 0.01$.

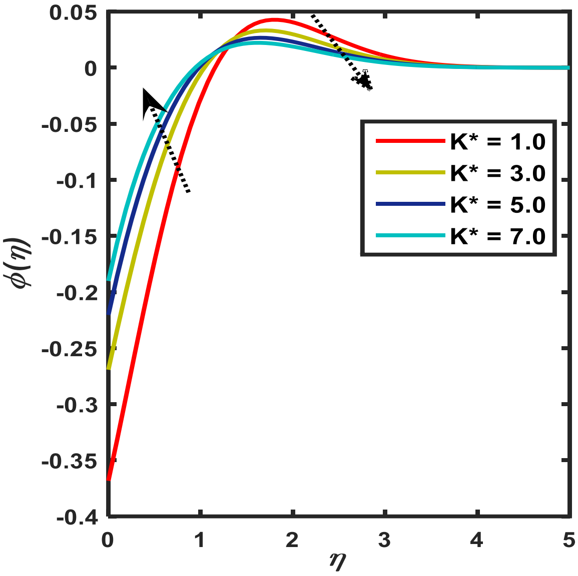

Fig. 7: ϕ profile for impact of chemical reaction with $M = 1.0, n = 1.0, Gr = 0.3, Gm = 0.3, \kappa = 0.1, Ec = 0.01, Rd = 0.01, Pr = 1.0, Nt = 0.2, Sc = 1.0, Q^* = 1.0, Nb = 0.2, A = 0.01, \delta_1 = 0.01, \delta_2 = 0.01, \delta_3 = 0.01, A_1 = 0.01$.

4.7 Influence of radiation (Rd)

Fig. 8 designates the impacts of the radiation parameter on the θ and ϕ profiles. In Fig. 8(a), the temperature (thermal BL thickness) profile increases for higher effects of the radiation parameter within the BL region. Furthermore, in Fig. 8(b), the concentration profile (concentration BL thickness) upsurges near the cylindrical surface and drops in distance from the surface within the BL region. These results can be explained by the fact that a decrease in the Rosseland radiation absorptivity is correlated with an increase in the radiation parameter. Consequently, the radiative heat flux divergence increases as Rosseland radiation absorptivity decreases. As a result, the fluid's temperature increases and its radiative heat transfer rate improves. A concentration gradient in the boundary layer brought on by intense external radiation moves the nanoparticles to the outer free stream region.

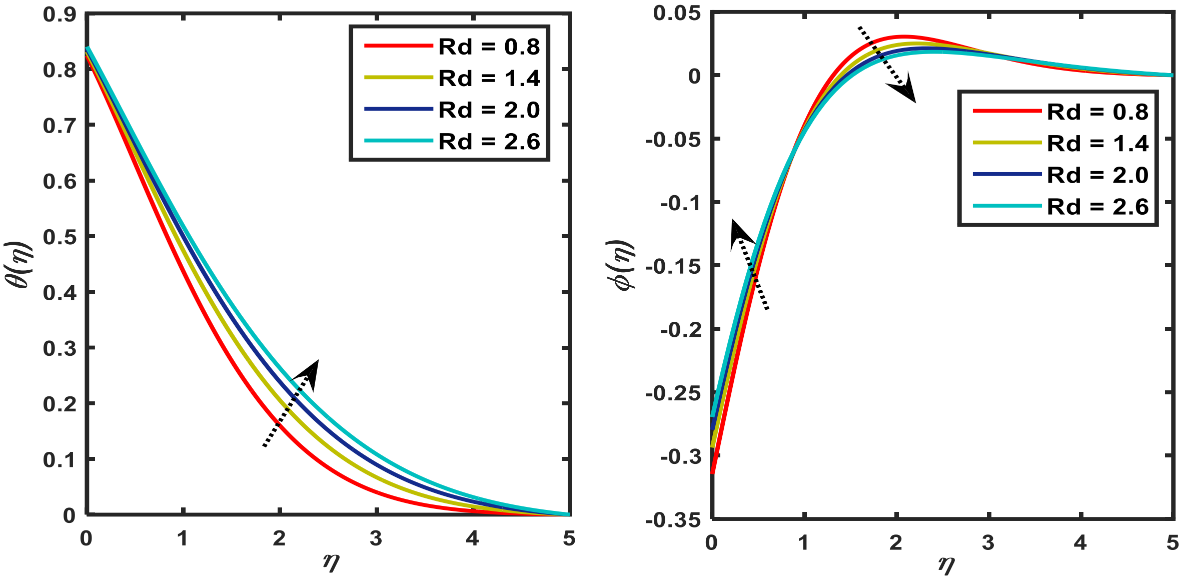

(a) (b)

Fig. 8: (a) θ , and (b) ϕ profiles for the impact of radiation $M = 1.0$, $n = 1.0$, $Gr = 0.3$, $Gm = 0.3$, $\kappa = 0.1$, $Ec = 0.01$, $Pr = 1.0$, $Nt = 0.2$, $Sc = 1.0$, $Q^* = 1.0$, $Nb = 0.2$, $A = 0.01$, $\delta_1 = 0.01$, $\delta_2 = 0.01$, $\delta_3 = 0.01$, $A_1 = 0.01$.

4.8 Influence of stretching ratio (A)

Fig. 9 illustrates the influences of the stretching ratio on f', θ, and ϕ profiles. Fig. 9(a) displays that f' rise for higher stretching ratio parameter values. Fig. 9(b) exemplifies that θ and thermal BL thickness decline for more significant impacts of the stretching ratio parameter. However, in Fig. 9(c), the concentration profile and concentration BL thickness increase close to the cylindrical surface and decline far away from the surface for higher values of the stretching parameter. From a physical point of view, boosting the stretching ratio parameter alters the fluid particle location, which improves the velocity field and increases the particle's mobility. On the other hand, a lower temperature results in a higher stretching ratio value. Free stream velocity is less than stretching velocity when A is small. A high stretching ratio parameter effectively raises the free stream velocity, which accelerates the rate at which heat moves from the wall to the free stream. The fluid concentration also drops with A due to the high free stream velocity.

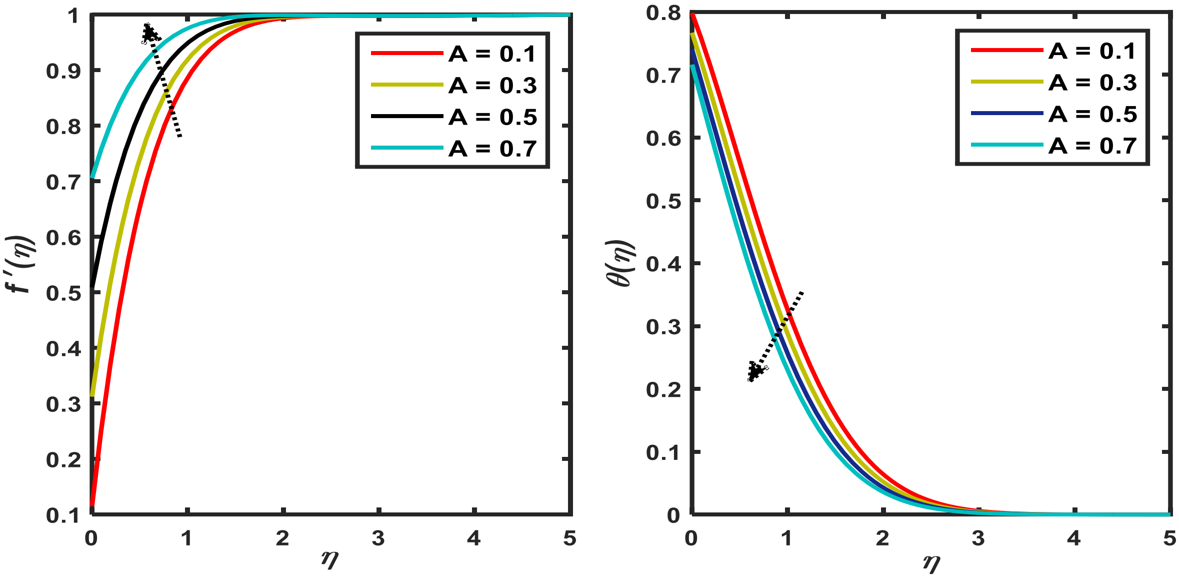

(a) (b)

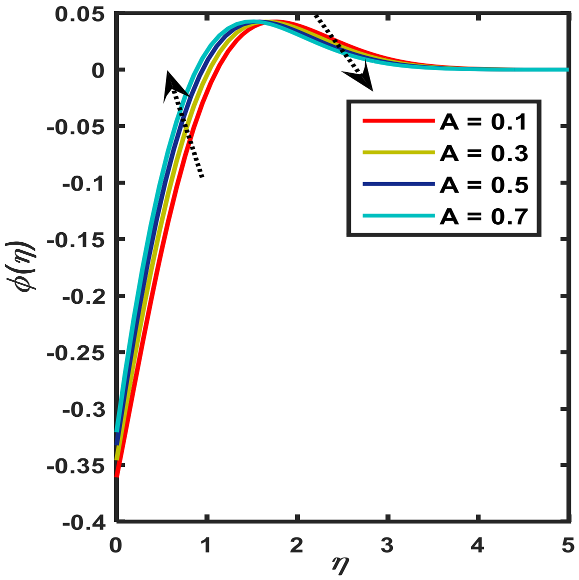

(c)

Fig. 9: (a) f', (b) θ, and (c) ϕ profiles for the impact of stretching ratio with $M = 1.0$, $Gr = 0.3$, $Gm = 0.3$, $\kappa = 0.1$, $Ec = 0.01$, $Rd = 0.01$, $Pr = 1.0$, $Nt = 0.2$, $Q^* = 1.0$, $Sc = 1.0$, $K^* = 1.0$, $Nb = 0.2$, $Bi = 2.0$, $n = 1.0$, $\delta_1 = 0.01$, $\delta_2 = 0.01$, $\delta_3 = 0.01$, $A_1 = 0.01$..

4.9 Influence of Biot number (*Bi*)

Fig. 10 portrays the behavior of the Biot number on θ, and ϕ profiles. Also, in Fig. 10(a), the temperature profile increases for higher values of the Biot number. However, in Fig. 10(b), the concentration profile and BL thickness drop near the cylinder and rise with increasing distance from the surface with increasing values of the Biot number. From a physical perspective, the Biot number illustrates the relationship between convective resistance at an object's surface and interior conductive resistance. To improve thermal energy expandability, buoyant force causes temperature, density, and fluid flow to increase. Because the strengthening of convection results in a decrease in the heat resistance of the cylindrical surface, the temperature of the cylindrical surface increases with more pronounced impacts of the Biot number.

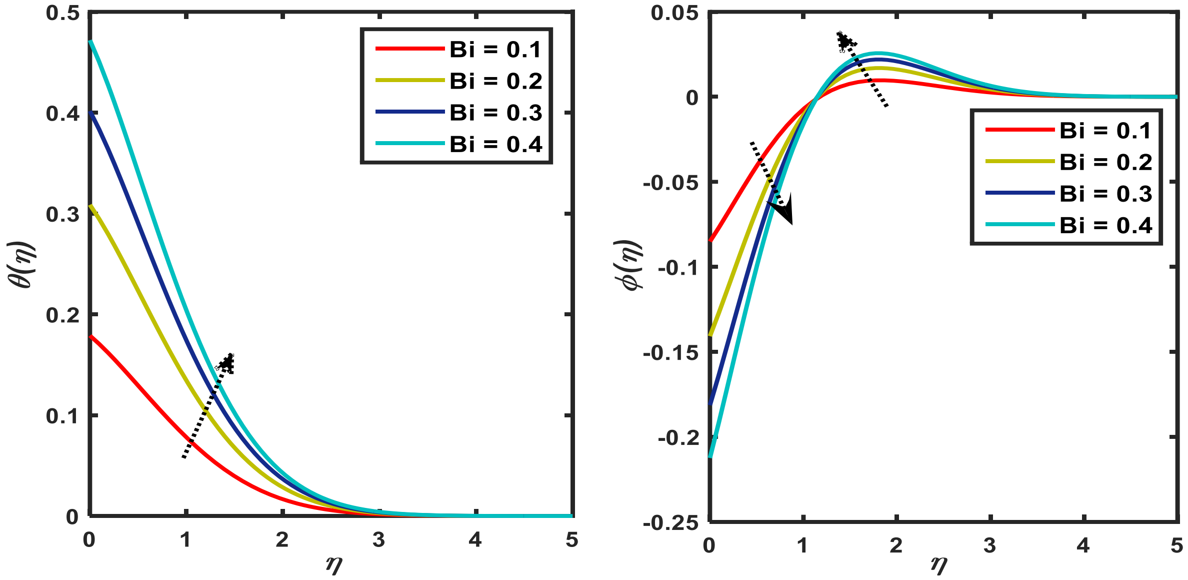

(a) (b)

Fig. 10: (a) θ, and (b) ϕ profiles for the impact of the Biot number with $M = 1.0$, $Gr = 0.3$, $Gm = 0.3$, $\kappa = 0.1$, $Ec = 0.01$, $Rd = 0.01$, $Pr = 1.0$, $Nt = 0.2$, $Q^* = 1.0$, $Sc = 1.0$, $K^* = 1.0$, $Nb = 0.2$, $A = 0.01$, $n = 1.0$, $\delta_1 = 0.01$, $\delta_2 = 0.01$, $\delta_3 = 0.01$, $A_1 = 0.01$.

4.10 Influence of Power-law index (*n*)

The impacts of the Power-law index on f', θ, and ϕ profiles are portrayed in Fig. 11. In Fig. 11(a), the velocity profile surges within the BL region for wider effects of n. Conversely, in Fig. 11(b), θ decays within the BL region occur for higher values of n. However, in Fig. 11(c), the concentration profile increases near the cylindrical surface and declines with distance from the surface for increasing values of n. The stretched velocity is linear and constant for n = 0 and n = 1, respectively. Nevertheless, the stretched velocity is nonlinear for any value of n > 1. According to the relationship, the stretched velocity's nonlinearity improves and, conversely, its velocity increases with bigger effects of n. However, for temperature, the opposite pattern is seen. The concentration approaches the distance from the surface due to the stretched surface; as a result, the thickness of the concentration boundary layer is lowered.

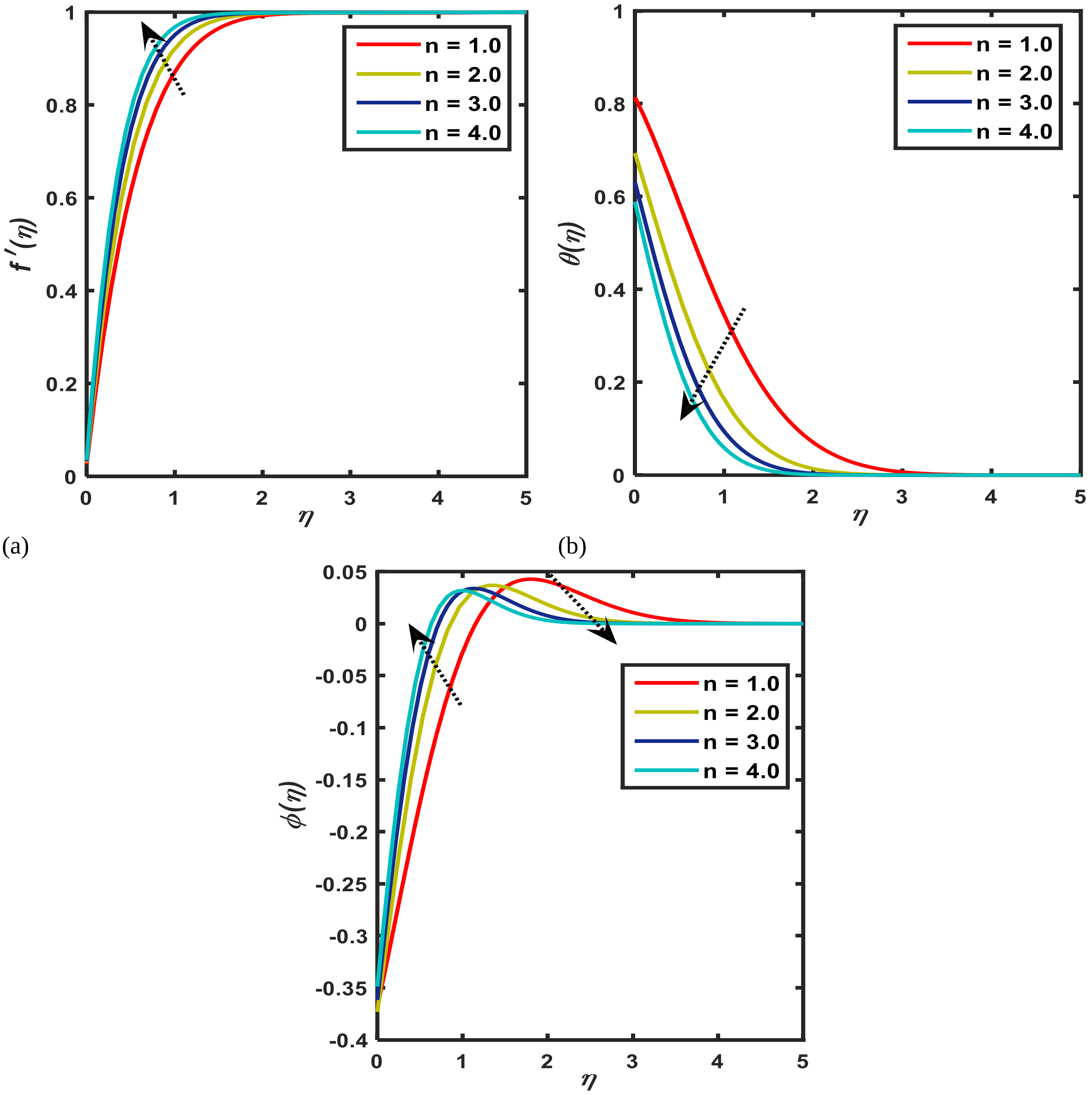

(a) (b)

(c)

Fig. 11: (a) f', (b) θ, and (c) ϕ profiles against the Power-law index (n) with $M = 1.0$, $Gr = 0.3$, $Gm = 0.3$, $\kappa = 0.1$, $Ec = 0.01$, $Rd = 0.01$, $Pr = 1.0$, $Nt = 0.2$, $Q^* = 1.0$, $Sc = 1.0$, $K^* = 1.0$, $Nb = 0.2$, $Bi = 2.0$, $A = 0.01$, $\delta_1 = 0.01$, $\delta_2 = 0.01$, $\delta_3 = 0.01$, $A_1 = 0.01$.

4.11 Influence of velocity slip (δ_1)

Fig. 12 signifies the consequences of the velocity slip parameter on velocity, temperature, and concentration profiles. Fig. 12(a) shows that the velocity profile enhances near the cylindrical surface for higher values of δ_1.

On the other hand, temperature profile and thermal BL thickness decline within BL region which is exemplified in Fig. 12(b) for growing values of the velocity slip parameter However, in Fig. 12(c), concentration profile and BL thickness enhances near the cylindrical surface and diminishes distance away from the surface within BL region for higher effects of velocity slip parameter. Physically, it is clear that during a slip, the fluid velocity near the sheet does not remain constant with the rate of surface stretching. In this instance, the slip component enhances the fluid's speed since it only partially draws the stretched surface. The fluid temperature decreases close to the BL when the velocity slip parameter is increased with a thermal jump and a magnetic field. There is more momentum transfer from the stretching sheet to the free stream, which results in a decrease in temperature and concentration. By doing this, the heat energy and nanoparticles are prevented from entering the free stream.

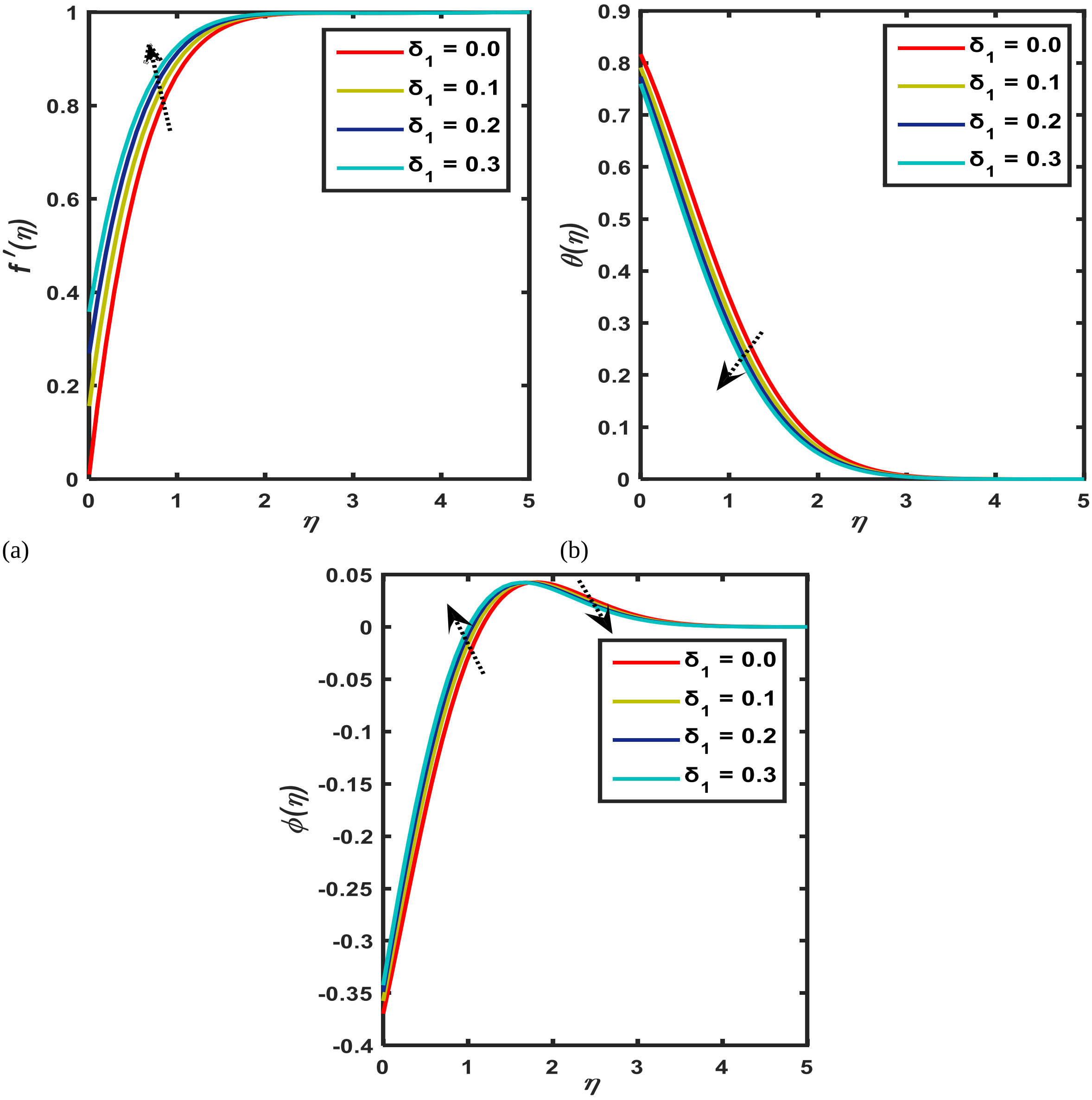

(a) (b)

(c)

Fig. 12: (a) f', (b) θ, and (c) ϕ profiles for the velocity slip with $M = 1.0$, $Gr = 0.3$, $Gm = 0.3$, $\kappa = 0.1$, $Ec = 0.01$, $Rd = 0.01$, $Pr = 1.0$, $Nt = 0.2$, $Q^* = 1.0$, $Sc = 1.0$, $K^* = 1.0$, $Nb = 0.2$, $Bi = 2.0$, $A = 0.01$, $n = 1.0$, $\delta_2 = 0.01$, $\delta_3 = 0.01$, $A_1 = 0.01$.

4.12 Influence of thermal slip (δ_2)

Fig. 13 shows the effects of the thermal slip on temperature and concentration profiles. In Fig. 13(a), the temperature profile and thermal BL thickness decline for higher values of the thermal slip. However, in Fig. 13(b), the concentration profile and BL thickness increase near the cylindrical surface and decrease far away from the surface for a higher value of the thermal slip parameter. From a physical perspective, the temperature within the flow can be resisted by the thermal slip parameter. The thermal BL thickness declines as the thermal slip increases, even with very little heat transfer from the fluid surface. Physically, temperature fields and the concentration profile exhibit a drop further from the surface because the highest thermal slip parameter strength reduces surface drag, which in turn reduces the amount of heat generated.

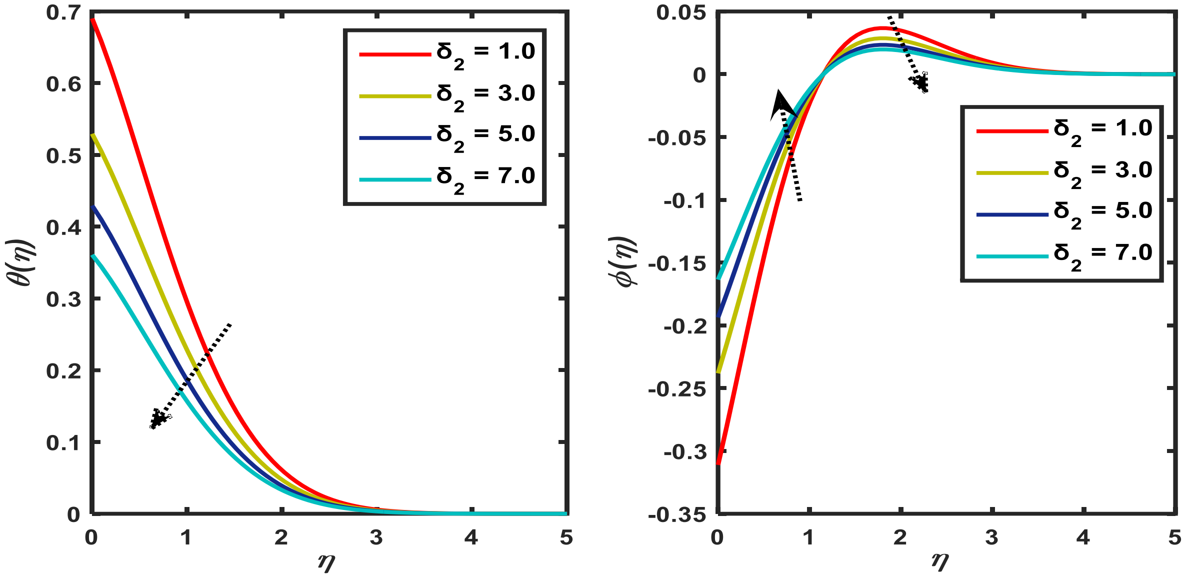

(a) (b)

Fig. 13: (a) θ , and (b) ϕ profiles for the impact of thermal slip with $M = 1.0$, $Gr = 0.3$, $Gm = 0.3$, $\kappa = 0.1$, $Ec = 0.01$, $Rd = 0.01$, $Pr = 1.0$, $Nt = 0.2$, $Q^* = 1.0$, $Sc = 1.0$, $K^* = 1.0$, $Nb = 0.2$, $Bi = 2.0$, $A = 0.01$, $n = 1.0$, $\delta_1 = 0.01$, $\delta_3 = 0.01$, $A_1 = 0.01$.

4.13 Influence of concentration slip (δ_3)

Fig. 14 portrays the influences of the concentration slip on the concentration profile. The concentration profile and BL thickness decrease for higher values of the concentration slip, as depicted in Fig. 14. Slip reduces fluid mobility, which in turn lowers net molecular movement. Consequently, the mass fraction fields decrease as molecular mobility decreases. A concentration slip in chemical kinetics is a reaction rate that is precisely proportional to the concentration of a single component. This implies that the half-life of the reaction is constant and that the rate of reaction also rises proportionately as the reactant concentration does. Concentration slips are crucial to many natural and man-made processes, including radioactive decay and certain chemical breakdowns.

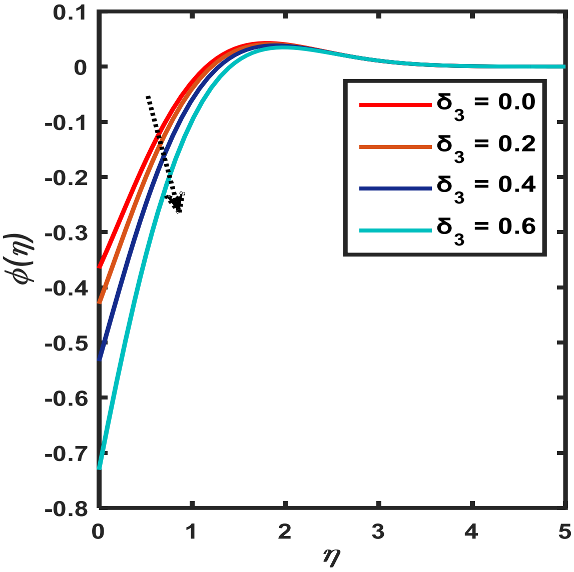

Fig. 14: ϕ profile for impact of concentration slip with $M = 1.0$, $Gr = 0.3$, $Gm = 0.3$, $\kappa = 0.1$, $Ec = 0.01$, $Rd = 0.01$, $Pr = 1.0$, $Nt = 0.2$, $Q^* = 1.0$, $Sc = 1.0$, $K^* = 1.0$, $Nb = 0.2$, $Bi = 2.0$, $A = 0.01$, $n = 1.0$, $\delta_1 = 0.01$, $\delta_2 = 0.01$, $A_1 = 0.01$.

4.14 Influence of unsteadiness (A_1)

Fig. 15 illustrates the impacts of unsteadiness on f', θ, and ϕ profiles. Fig. 15(a) displays that velocity decreases, and the momentum BL thickness & skin friction coefficient increase. In contrast, the opposite behavior is observed for the temperature and concentration profiles, shown in Figs. 15(b) and 15(c). From a physical point of view, due to the stretching sheet, the instability parameter reduces the flow rate, which reduces the fluid's velocity, temperature, and density.

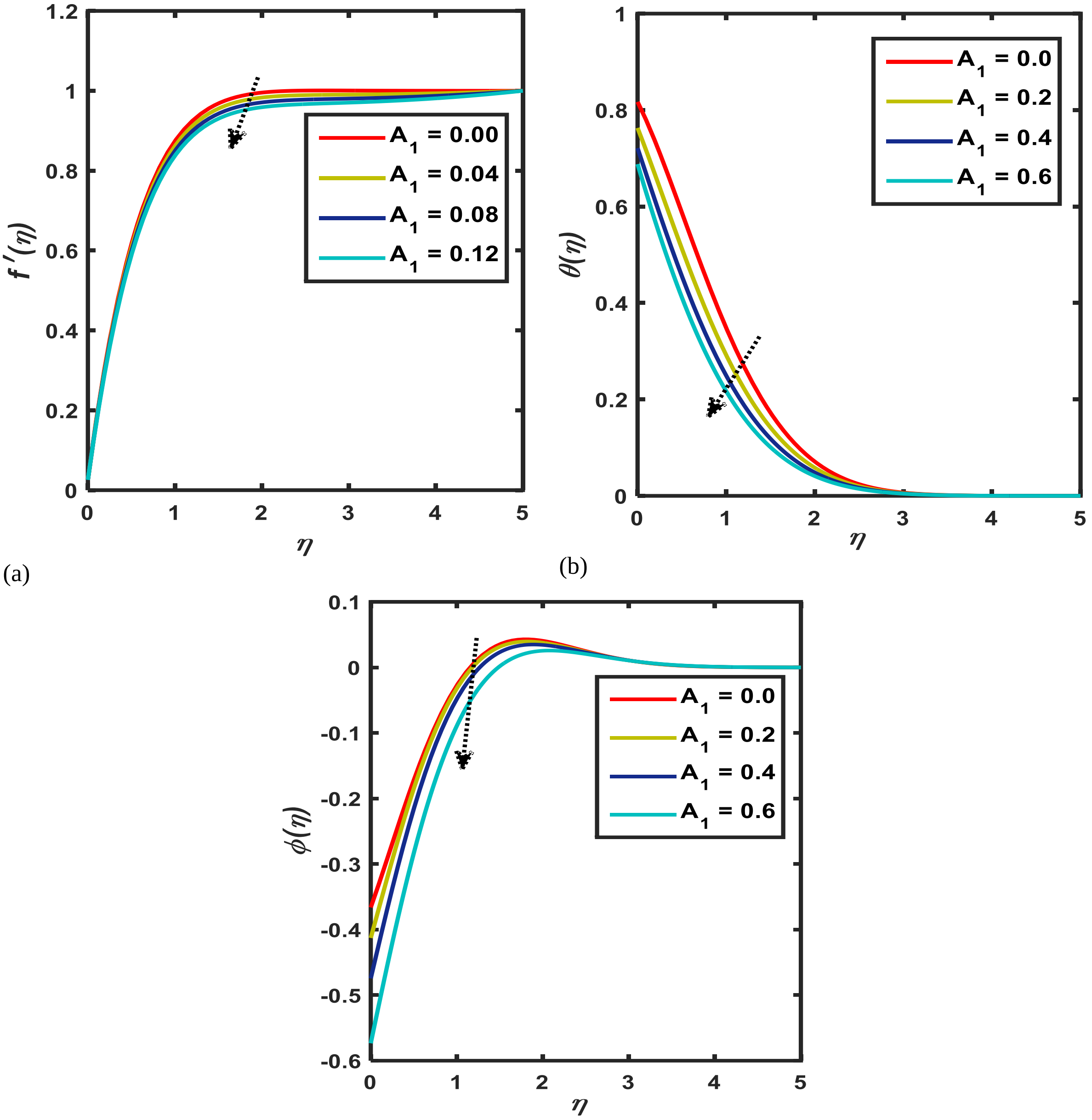

(a)

(b)

(c)

Fig. 15: (a) f', (b) θ, and (c) ϕ profiles for different values of unsteadiness with $M = 1.0$, $Gr = 0.3$, $Gm = 0.3$, $\kappa = 0.1$, $Ec = 0.01$, $Rd = 0.01$, $Pr = 1.0$, $Nt = 0.2$, $Q^* = 1.0$, $Sc = 1.0$, $K^* = 1.0$, $Nb = 0.2$, $Bi = 2.0$, $A = 0.01$, $n = 1.0$, $\delta_1 = 0.01$, $\delta_2 = 0.01$, $\delta_3 = 0.01$.

In Table 1, it is observed that the decreasing rate of skin friction coefficient is higher in unsteady flow than steady flow for the effects of M, n, κ and lower for Gr. Furthermore, the increasing rate of skin friction coefficient is higher in unsteady flow than steady flow for the effects of Gm, A, and lower for δ_1.

Table 1: Values of skin friction coefficient in steady and unsteady flow due to M, n, Gr, Gm, κ, A, δ_1 variations with $Ec = 0.01, Rd = 0.01, Pr = 1.0, Nt = 0.2, Q^* = 1.0, Sc = 1.0, K^* = 1.0, Nb = 0.2, Bi = 2.0, \delta_2 = 0.01$, $\delta_3 = 0.01$.

M	n	Gr	Gm	κ	A	δ_1	$f''(0)$ (Steady flow)	$f''(0)$ (Unsteady flow)
0.0	1.0	0.3	0.3	0.1	0.01	0.01	-1.3538	-1.3462
3.0							-2.1170	-2.1125
6.0							-2.6561	-2.6525
9.0							-3.0945	-3.0913
1.0	1.0	0.3	0.3	0.1	0.01	0.01	-1.6513	-1.6453
	2.0						-1.9885	-1.9840
	3.0						-2.2811	-2.2772
	4.0						-2.5395	-2.5359
1.0	1.0	0.3	0.3	0.1	0.01	0.01	-1.6513	-1.6453
		1.3					-1.9687	-1.9608
		2.3					-2.2539	-2.2447
		3.3					-2.5167	-2.5065
1.0	1.0	0.3	0.3	0.1	0.01	0.01	-1.6513	-1.6453
			3.3				-1.3195	-1.3123
			6.3				-0.9431	-0.9344
			9.3				-0.4737	-0.4627
1.0	1.0	0.3	0.3	0.0	0.01	0.01	-1.6394	-1.6333
				0.2			-1.6633	-1.6574
				0.4			-1.6864	-1.6805
				0.6			-1.7073	-1.7015
1.0	1.0	0.3	0.3	0.1	0.1	0.01	-1.5282	-1.5222
					0.3		-1.2376	-1.2315
					0.5		-0.9246	-0.9183
					0.7		-0.5901	-0.5838
1.0	1.0	0.3	0.3	0.1	0.1	0.0	-1.6737	-1.6676
						0.1	-1.4689	-1.4635
						0.2	-1.3016	-1.2968
						0.3	-1.1648	-1.1606

Table 2: Values of Nusselt number in steady and unsteady flow due to n, κ, Ec, Rd, Pr, Nt, Nb, Q*, Bi, A, δ_2 variations with $M = 1.0, n = 1.0,\ Gr = 0.3, Gm = 0.3, \kappa = 0.1, Sc = 1.0, K^* = 1.0, Nb = 0.2, Bi = 2.0, \delta_1 = 0.01, \delta_3 = 0.01$.

n	κ	Ec	Rd	Pr	Nt	Nb	Q*	Bi	A	δ_2	$\theta'(0)$ (Steady flow)	$\theta'(0)$ (Unsteady flow)
1.0	0.1	0.01	0.01	1	0.2	0.2	1	2	0.01	0.01	0.3624	0.3685
2.0											0.6039	0.6064
3.0											0.7288	0.7303
4.0											0.8134	0.8145
	0.0	0.01	0.01	1	0.2	0.2	1	2	0.01	0.01	0.2802	0.2878
	0.2										0.4295	0.4345
	0.4										0.5310	0.5346
	0.6										0.6034	0.6061
	0.1	0.0	0.01	1	0.2	0.2	1	2	0.01	0.01	0.3567	0.6009
		0.5									0.6333	0.8566
		1.0									0.8926	1.1031
		1.5									1.1349	1.3396
	0.1	0.01	0.8	1	0.2	0.2	1	2	0.01	0.01	0.3442	0.3481
			1.4								0.3313	0.3345
			2.0								0.3214	0.3242
			2.6								0.3138	0.3163

n	κ	Ec	Rd	Pr	Nt	Nb	Q*	Bi	A	δ_2	$\theta'(0)$ (Steady flow)	$\theta'(0)$ (Unsteady flow)
	0.1	0.01	0.01	0.15	0.2	0.2	1	2	0.01	0.01	0.2999	0.3018
				0.25							0.3176	0.3202
				0.35							0.3311	0.3343
				0.45							0.3411	0.3448
	0.1	0.01	0.01	1	0.1	0.2	1	2	0.01	0.01	0.3576	0.3638
					0.2						0.3624	0.3685
					0.3						0.3669	0.3728
					0.4						0.3710	0.3767
	0.1	0.01	0.01	1	0.2	0.1	1	2	0.01	0.01	0.3595	0.3656
						0.2					0.3624	0.3685
						0.3					0.3634	0.3694
						0.4					0.3638	0.3699
	0.1	0.01	0.01	1	0.2	0.2	0.0	2	0.01	0.01	0.6470	0.6496
							0.3				0.5835	0.5867
							0.6				0.5049	0.5090
							0.9				0.4034	0.4089
	0.1	0.01	0.01	1	0.2	0.2	1	0.1	0.01	0.01	0.0810	0.0813
								0.2			0.1360	0.1369
								0.3			0.1762	0.1777
								0.4			0.2070	0.2092
	0.1	0.01	0.01	1	0.2	0.2	1	2	0.1	0.01	0.3941	0.3998
									0.3		0.4569	0.4617
									0.5		0.5110	0.5152
									0.7		0.5585	0.5622
	0.1	0.01	0.01	1	0.2	0.2	1.0	2	0.1	1	0.3053	0.3097
										3	0.2326	0.2353
										5	0.1884	0.1902
										7	0.1585	0.1598

From Table 2, it is seen that the increasing rate of Nusselt number is lower in unsteady flow than in steady flow for the effects of *n*, *Ec*, κ, *Nb*, *Nt*, *A*, and higher for Pr, *Bi*. Additionally, the decreasing rate of Nusselt number is higher in unsteady flow than steady flow for the different values of *Rd*, *Q**, and δ_2.

Table 3: Values of Sherwood number in steady and unsteady flow due to n, κ, Nt, Nb, Sc, K*, and δ_3 variations with $M = 1.0, Gr = 0.3, Gm = 0.3, Ec = 0.01, Rd = 0.01, Pr = 1.0, Nt = 0.2, Q^* = 1.0, Bi = 2.0, A = 0.01, \delta_1 = 0.01, \delta_2 = 0.01$.

n	κ	Nt	Nb	Sc	K*	δ_3	$\phi'(0)$ (Steady flow)	$\phi'(0)$ (Unsteady flow)
1.0	0.1	0.2	0.2	1.0	1.0	0.01	- 0.3661	- 0.3722
2.0							- 0.6100	- 0.6125
3.0							- 0.7361	- 0.7377
4.0							- 0.8216	- 0.8227
1.0	0.0	0.2	0.2	1.0	1.0	0.01	- 0.2831	- 0.2907
	0.2						- 0.4338	- 0.4389
	0.4						- 0.5364	- 0.5400
	0.6						- 0.6095	- 0.6122
1.0	0.1	0.1	0.2	1.0	1.0	0.01	- 0.1806	- 0.1837
		0.2					- 0.3661	- 0.3722
		0.3					- 0.5559	- 0.5648
		0.4					- 0.7494	- 0.7611
1.0	0.1	0.2	0.1	1.0	1.0	0.01	- 0.7262	- 0.7386
			0.2				- 0.3661	- 0.3722
			0.3				- 0.2447	- 0.2488
			0.4				- 0.1838	- 0.1868
1.0	0.1	0.2	0.2	1.0	1.0	0.01	- 0.3661	- 0.3722

n	κ	Nt	Nb	Sc	K*	δ_3	$\phi'(0)$ (Steady flow)	$\phi'(0)$ (Unsteady flow)
				2.0			- 0.3718	- 0.3778
				3.0			- 0.3749	- 0.3809
				4.0			- 0.3769	- 0.3829
1.0	0.1	0.2	0.2	1.0	1.0	0.01	- 0.3661	- 0.3722
					3.0		- 0.3729	- 0.3791
					5.0		- 0.3764	- 0.3825
					7.0		- 0.3786	- 0.3847
1.0	0.1	0.2	0.2	1.0	1.0	0.0	- 0.3626	- 0.3687
						0.2	- 0.4480	- 0.4555
						0.4	- 0.5860	- 0.5959
						0.6	- 0.8471	- 0.8614

Table 3 shows that the decreasing rate of Sherwood number is lower in unsteady flow than in steady flow for the different values of n, κ, *Nt*, *Sc*, and higher for δ_3. Conversely, the increasing rate of Sherwood number is lower in unsteady flow than in steady flow for the different values of *Nb*, and *K**.

5. Concluding Remarks

The study compares the behavior of nanofluid flow under steady flow conditions with that under time-varying (unsteady) flow conditions. The study considers how different slip effects, such as velocity and thermal slips, affect flow and heat transmission with thermal radiation, chemical reaction, and magnetic effects. The following summarizes the noteworthy findings of the analysis above:

- The skin friction coefficient in unsteady flow increases by 1.05%, 0.34%, 0.04%, 0.57%, and 0.26% respectively due to the upsurge of magnetic strength, power-law index, curvature, mass Grashof number, and stretching ratio compared to steady flow; as well as decreases by 0.07%, and 0.01% respectively due to the enhance of thermal Grashof number, and velocity slip.
- Compared to steady flow, for increasing values of power-law index, curvature, Eckert number, thermophoresis, Brownian motion, and stretching ratio, the Nusselt number in unsteady flow decreases by approximately 3.42%, 4.75%, 95.24%, 0.2%, 0.02%, and 1.1%; as well as increases by 0.3%, 0.51%, 0.6%, and 0.32% approximately for higher values of radiation, Prandtl number, heat generation, and, thermal slip.
- Increasing values of power-law index, curvature, thermophoresis, Brownian motion, Schmidt number, and chemical reaction decrease the Sherwood number in unsteady flow by about 3.38%, 4.69%, 0.63%, 0.02%, 0.08%, and 0.05%, respectively, compared to steady flow; as well as increase in unsteady flow by 0.01% for increasing values of concentration slip.
- The power-law index, magnetic strength, and stretching ratio act as controlling factors because the mass transfer rate declines in the BL region, but the fluid velocity and heat transfer rate increase.
- Brownian motion, thermophoresis, heat generation, radiation, magnetic fields, stretching ratio, power-law index, velocity slip, thermal slip, Schmidt number, and chemical reaction have an oscillatory relationship with the concentration profile.

From the perspective of MHD flow, this analysis is essential to comprehending the comparison of steady and unsteady flows of nanofluid and their uses in thermal engineering systems, including electronics cooling, nuclear reactors, energy systems, solar thermal systems, biomedical applications, the petroleum industry, and chemical processing where enhanced thermal behavior is essential.

References

Abbas, N., Nadeem, S., Saleem, A., Malik, M. Y., Issakhov, A., and Alharbi, F.M. (2021): Models base study of inclined MHD of hybrid nanofluid flow over nonlinear stretching cylinder, Chinese Journal of Physics, 69, 109-117, https://doi.org/10.1016/j.cjph.2020.11.019.

Abbas, N., Shatanawi, W., Abodayeh, K., and Shatnawi, T. A. M. (2023): Comparative analysis of unsteady of induced MHD radiative Sutterby fluid flow at nonlinear stretching cylinder/sheet: Variable thermal conductivity, Alexandria Engineering Journal, 72, 451-461, https://doi.org/10.1016/j.aej.2023.04.016.

Ahmed, S.E., Hussein, A.K., Mohammed, H. A., and Sivasankaran, S. (2014): Boundary layer flow and heat transfer due to permeable stretching tube in the presence of heat source/sink utilizing nanofluids, Applied Mathematics and Computation, 238, 149–162, https://doi.org/10.1134/S1810232814030059.

Ali, R.I. (2020): A review on nanofuid: preparation, stability, thermophysical properties, heat transfer characteristics and application, SN Applied Sciences, 17, 1636, https://doi.org/10.1007/s42452-020-03427-1.

Ali, M., Nasrin, R., and Alim, M. A. (2021): Analysis of boundary layer nanofluid flow over a stretching permeable wedge-shaped surface with magnetic effect, Journal of Naval Architecture and Marine Engineering, 18(1) 11-24, https://dx.doi.org/10.3329/jname.v18i1.44458.

Ali, M., Nasrin R., and Alim, M. A. (2023): Axisymmetric boundary layer slip flow with heat transfer over an exponentially stretching bullet-shaped object: A numerical assessment, Heliyon, 9(3), e13671, https://doi.org/10.1016/j.heliyon.2023.e13671.

Alia, R., Iqbal, A., Abbass, T., Arshad, T., and Shahzad, A. (2024): Unsteady flow of silica nanofluid over a stretching cylinder with effects of different shapes of nanoparticles and Joule heating, 45(3), 115–126, https://doi.org/10.24425/ather.2024.151222.

Bachok, N., Ishak, A., and Pop, I. (2012): Unsteady boundary-layer flow and heat transfer of a nanofluid over a permeable stretching/shrinking sheet, International Journal Heat & Mass Transfer, 55, 2102-2109, https://doi.org/10.1016/j.ijheatmasstransfer.2011.12.013.

Basit, M. A., Imran, M., Tahir, M., Eladeb, A. and Kolsi. L. (2024): Numerical analysis of mathematical model for heat and mass transfer through Bioconvective Maxwell nanofluid flow subject to Darcy-Forcheimer and Lorentz forces, International Journal of Heat and Fluid Flow, 106(10), https://doi.org/10.1016/j.ijheatfluidflow.2024.109322.

Bhargavi, N., Sreenivasulu, P., and Poornima, T. (2024): Comparative analysis on single- and multi-walled carbon nanotubes suspended for enhanced thermal energy transfer past stretching surfaces, AIP Advances, 14, 115124, https://doi.org/10.1063/5.0232829.

Bilal, M., Ishfaq, T., Lone, S.A., and Mehmood, Y. (2024): A numerical simulation of the unsteady MHD nanofluid flow over a rotating disk in a porous medium with uniform suction and convective effects, International Journal of Ambient Energy, 45(1), https://doi.org/10.1080/01430750.2024.2410924.

Buongiorno, J. (2006): Convective transport in nanofluids, Journal of Heat Transfer, 128, 240–250, https://doi.org/10.1115/1.2150834.

Chamkha, A. J., Rashad, A. M., and Aly, A. M. (2013): Transient natural convection flow of a nanofluid over a vertical cylinder, Meccanica, 48, 71–81, https://doi.org/10.1007/s11012-012-9584-8.

Choi, S.U.S. (1995): Enhancing thermal conductivity of fluids with nanoparticles, developments and applications of non-Newtonian flows, in: D.A. Siginer, H.P. Wang (Eds.), The American Society of Mechanical Engineers, 66, 99–105.

Choudhary, P., Choudhary, S., Jat, K., Loganathan, K., and Eswaramoorth, S. (2024): Impacts of unsteady MHD hybrid nanofluid over a non-linear stretchable porous sheet with thermal radiation and gyrotactic microorganisms, International Journal of Thermofluids, 23, 100788, https://doi.org/10.1016/j.ijft.2024.100788.

Dzulkifli, N.F., Bachok, N., Yacob, N.A., Arifin, N., Rosali, H., and Pop, I. (2021): Unsteady boundary layer flow over a permeable stretching/shrinking cylinder immersed in nanofluid, Journal of Advanced Research in Fluid Mechanics and Thermal Sciences, 85(2), 24-32, https://doi.org/10.37934/arfmts.85.2.2432

Elbashbeshy, E. M. A., Asker, H. G., and Nagy, B. (2022): The effects of heat generation absorption on boundary layer flow of a nanofluid containing gyrotactic microorganisms over an inclined stretching cylinder, Ain Shams Engineering Journal, 13(5), 101690, https://doi.org/10.1016/j.asej.2022.101690.

Gholinia, M., Gholinia, S., Hosseinzadeh, K., and Ganji, D.D. (2018): Investigation on ethylene glycol nanofluid flow over a vertical permeable circular cylinder under the effect of magnetic field, Results in Physics, 9, 1525–1533, https://doi.org/10.1016/j.rinp.2018.04.070.

Hossain, Md. M., Nasrin, R. and Molla, Md. M. (2025): Surface couple stress, thermal transfer, skin friction, and material transport by micropolar binary mixture: An in-depth computational analysis, Arabian Journal for Science and Engineering, https://doi.org/10.1007/s13369-025-10107-y.

Jalili, B., Emad, M., Jalili, P., Ganji, D.D., Saleem, S. and Tag-eldin, E.M. (2023): Thermal analysis of boundary layer nanofluid flow over the movable plate with internal heat generation, radiation, and viscous dissipation, Case Studies in Thermal Engineering, 49, 103203, https://doi.org/10.1016/j.csite.2023.103203.

Jarwal, V. K., Choudhary, S., and Sinha, S. (2023): Mixed convection boundary layer nanofluid flow over an inclined stretching cylinder with thermal radiation, International Journal of Development Research, 13(3), 61935-61944, https://doi.org/10.37118/ijdr.26371.03.2023.

Khan, Z., Khan, W., Arko, Y., Egami, RH., and Garalleh, HAL. (2025): Numerical stability of magnetized Williamson nanofluid over a stretching/shrinking sheet with velocity and thermal slips effect, Numerical Heat Transfer, Part B: Fundamentals, 86(6), 1763-1783, https://doi.org/10.1080/10407790.2024.2321483.

Mabood, F., and Shateyi, S. (2019): Multiple slip effects on MHD unsteady flow heat and mass transfer impinging on permeable stretching sheet with radiation, Modelling and Simulation in Engineering, 2019, 3052790, https://doi.org/10.1155/2019/3052790 .

Mansur, S., and Ishak, A. (2016): Unsteady boundary layer flow of a nanofluid over a stretching/shrinking sheet with a convective boundary condition, Journal of the Egyptian Mathematical Society, 24(4), 650-655, https://doi.org/10.1016/j.joems.2015.11.004.

Narender, G., Govardhan, K., and Sarma, G. S. (2021): Viscous dissipation and thermal radiation effects on the flow of Maxwell nanofluid over a stretching surface, International Journal of Nonlinear Analysis and Application, 12(2), 1267-1287, https://doi.org/10.22075/ijnaa.2020.18958.2045.

Nandi, S. and Barman, D. (2024): Unsteady MHD hybrid nanofluid flow over a convectively heated linear stretching cylinder with velocity slip: A comparative study, International Journal of Modern Physics B, 38(21), 2450284. https://doi.org/10.1142/S0217979224502849.

Poornima, T., Sreenivasulu, P., and Reddy B. N. (2016): Chemical reaction effects on an unsteady MHD mixed convective and radiative boundary layer flow over a circular cylinder, Journal of Applied Fluid Mechanics, 9(6), 2877-2885, https://doi.org/10.29252/jafm.09.06.24248.

Poornima, T., Sreenivasulu, P., and Souayeh, B. (2022): Mathematical study of heat transfer in a stagnation flow of a hybrid nanofluid over a stretching/shrinking cylinder. Journal of Engineering Physics and Thermophysics, 95, 1443–1454, https://doi.org/10.1007/s10891-022-02613-9.

Rajput, S., Bhattacharyya, K., Pandey, A. K., and Chamkha, A. J. (2022): Unsteady axisymmetric flow of nanofluid on nonlinearly expanding surface with variable fluid properties, JCIS Open, 8, 100064, https://doi.org/10.1016/j.jciso.2022.100064.

Reddy, G.J., Hiremath, A., and Kumar, M. (2018): Computational modeling of unsteady third-grade fluid flow over a vertical cylinder: A study of heat transfer visualization. Results in Physics, 8, 671–682, https://doi.org/10.1016/j.rinp.2017.12.054.

Reddy, R. C. S., and Reddy, P. S. (2020): A comparative analysis of unsteady and steady Buongiorno's Williamson nanoliquid flow over a wedge with slip effects, Chinese Journal of Chemical Engineering, 28, 1767-1777, https://doi.org/10.1016/j.cjche.2020.04.016

Revathi, R., and Poornima, T. (2024): Unsteady convection and Stefan blowing influence on Sutterby nanofluid past stretching surface, BioNanoScience, 14(3), 1-16, https://doi.org/10.1007/s12668-024-01427-8.

Rosseland, S. (1931): Astrophysik und Atom-Theoretische Grundlagen, Springer Verlag, Berlin, 41, https://doi.org/10.1007/978-3-662-26679-3.

Saranya, S., Ragupathi, P., and Al-Mdallal, Q.M. (2024): Thermal and reactive effects in nanofluid flow around a contracting cylinder under magnetic field influence, International Journal of Thermofluids, 22, 100710, https://doi.org/10.1016/j.ijft.2024.100710.

Shatnawi, T. A. M., Abbas, N., and Shatanawi, W. (2022): Comparative study of Casson hybrid nanofluid models with induced magnetic radiative flow over a vertical permeable exponentially stretching sheet, AIMS Mathematics, 7(12), 20545-20564, https://doi.org/10.3934/math.20221126.

Tulapurkara, E.G. (2005): Hundred years of the boundary layer, Sadhana, 30(4), 499-512, https://doi.org/10.1007/BF02703275.

Tulu, A., Asefa, L. and Sohail, M. (2024): Unsteady magnetohydrodynamic hybrid nanofluid flow over a rotating disk with viscous dissipation and Cattaneo–Christov heat flux model, International Journal of Thermofluids, 21, 100586, https://doi.org/10.1016/j.ijft.2024.100586.

Uddin, M. J., Nasrin, R., and Alatawi, E. S. (2025): Stability analysis of unsteady oriented magneto-convective porous medium: Exploring boundary-layer flow dynamics through regression modeling, Heat Transfer,n2025, 1–34, https://doi.org/10.1002/htj.23347.

Uddin, M. J., Nasrin, R. and Alatawi, E. S. (2025): Augmenting thermal-material transport in boundary-layer flow over an upright sheet: An explicit finite difference approach, Journal of Naval Architecture and Marine Engineering, 22(1), 21-40, https://doi.org/10.3329/jname.v22i1.77636.

Umeshaiah, M., Madhukesh, J., Khan, U., Rana, S., Zaib, A., Raizah, Z., and Galal, A. M. (2022): Dusty nanoliquid flow through a stretching cylinder in a porous medium with the influence of the melting effect, Processes, 10, 1065, https://doi.org/10.3390/pr10061065.

Waqas, H., Yasmin, S., Muhammad, T. and Imran, M. (2021): Flow and heat transfer of nanofluid over a permeable cylinder with nonlinear thermal radiation, Journal of Materials Research and Technology, 14, 2579-2585, https://doi.org/10.1016/j.jmrt.2021.07.030 .

Zeeshan, M. E.E., Khan, W., Saleem, S., Kallel, M., and Radwan, N. (2025): Stability analysis of Casson hybrid nanofluid in a rocket engine nozzle with Cattaneo-Christov heat flux and velocity slip effects, ZAMM-Journal of Applied Mathematics and Mechanics, 105(5), e70103, https://doi.org/10.1002/zamm.70103 .